

THE MILKY WAY IMAGING SCROLL PAINTING (MWISP): PROJECT
DETAILS AND INITIAL RESULTS FROM THE GALACTIC LONGITUDE OF
+25°8 TO +49°7

YANG SU,¹ JI YANG,¹ SHAOBO ZHANG,¹ YAN GONG,^{1,2} HONGCHI WANG,¹
XIN ZHOU,¹ MIN WANG,¹ ZHIWEI CHEN,¹ YAN SUN,¹ XUEPENG CHEN,¹ YE XU,¹
AND ZHIBO JIANG¹

¹*Purple Mountain Observatory and Key Laboratory of Radio Astronomy, Chinese Academy of Sciences, Nanjing 210034, China*

²*Max-Planck Institute für Radioastronomie, Auf dem Hügel 69, 53121 Bonn, Germany*

ABSTRACT

The Milky Way Imaging Scroll Painting (MWISP) project is an unbiased Galactic plane CO survey for mapping regions of $l = -10^\circ$ to $+250^\circ$ and $|b| \lesssim 5^\circ 2$ with the 13.7 m telescope of the Purple Mountain Observatory. The legacy survey aims to observe the ^{12}CO , ^{13}CO , and C^{18}O ($J=1-0$) lines simultaneously with full-sampling using the nine-beam Superconducting Spectroscopic Array Receiver (SSAR) system with an instantaneous bandwidth of 1 GHz. In this paper, the completed 250 deg² data from $l = +25^\circ 8$ to $+49^\circ 7$ are presented with a grid spacing of $30''$ and a typical rms noise level of ~ 0.5 K for ^{12}CO at the channel width of 0.16 km s^{-1} and ~ 0.3 K for ^{13}CO and C^{18}O at 0.17 km s^{-1} . The high-quality data with moderate resolution ($\sim 50''$), uniform sensitivity, and high spatial dynamic range, allow us to investigate the details of molecular clouds (MCs) traced by the three CO isotope lines. Three interesting examples are briefly investigated, including distant Galactic spiral arms traced by CO emission with $V_{\text{LSR}} < 0 \text{ km s}^{-1}$, the bubble-like dense gas structure near the H II region W40, and the MCs distribution perpendicular to the Galactic plane.

Keywords: Galaxy: structure – ISM: clouds – ISM: molecules – radio lines: ISM – stars: formation – surveys

1. INTRODUCTION

Molecular gas plays a crucial role in star formation. Molecular hydrogen (H_2) is the dominant component of molecular clouds (MCs) in the interstellar medium (ISM). Unfortunately, H_2 radiates inefficiently in the cold, dense molecular ISM due to a lack of a permanent dipole moment and corresponding dipolar rotational transitions in the radio band (e.g., [Bolatto et al. 2013](#)). Carbon monoxide (CO), which is the next most abundant molecule in the ISM, is widely used to trace the molecular gas because CO emission is easily excited in the molecular ISM environment and the CO $J=1-0$ transition at 2.6 mm (or 115 GHz) is readily observed on the ground (e.g., [Combes 1991](#); [Dame et al. 2001](#); [Heyer & Dame 2015](#) and references therein).

Systematic CO surveys of the Milky Way are helpful for improving our knowledge of the molecular ISM, the physics of star formation, and the Galactic structures. So far, many Galactic CO surveys have been done using single-dish telescopes, such as the FCRAO ^{12}CO ($J=1-0$) survey of the Outer Galaxy ([Heyer et al. 1998](#)), the CfA 1.2 m complete ^{12}CO ($J=1-0$) survey (see Figure 1 and Table 1 in [Dame et al. 2001](#)), the Bell Laboratories 7 m ^{13}CO ($J=1-0$) survey ([Lee et al. 2001](#)), the NANTEN 4 m ^{12}CO ($J=1-0$) survey ([Mizuno & Fukui 2004](#)), the FCRAO 14 m ^{13}CO ($J=1-0$) Galactic Ring Survey (GRS, [Jackson et al. 2006](#)), the Mopra 22 m ^{12}CO , ^{13}CO , C^{18}O ($J=1-0$) survey ([Burton et al. 2013](#)), and the Three-mm Ultimate Mopra Milky Way Survey (ThrUMMS) for ^{12}CO , ^{13}CO , C^{18}O , and CN ($J=1-0$) lines ([Barnes et al. 2015](#)).

Detailed information for large CO surveys was summarized in Figures 1–2 in [Heyer & Dame \(2015\)](#), in which the authors enumerate the major surveys of ^{12}CO and ^{13}CO ($J=1-0$) emission along the Galactic plane from 1970–2015. The FOREST Unbiased Galactic plane Imaging survey with the Nobeyama 45 m telescope (FUGIN; [Umamoto et al. 2017](#)) plans to conduct the simultaneous ^{12}CO , ^{13}CO , and C^{18}O ($J=1-0$) observations toward the Galactic plane. This survey will achieve rather high angular resolution ($\sim 20''$) data of CO ($J=1-0$) lines for the Galactic plane.

The ^{12}CO ($J=3-2$) High-Resolution Survey of the Galactic plane (COHRS, [Dempsey et al. 2013](#)) and the $^{13}\text{CO}/\text{C}^{18}\text{O}$ ($J=3-2$) Heterodyne Inner Milky Way Plane Survey (CHIMPS, [Rigby et al. 2016](#)) were made using the 15 m James Clerk Maxwell Telescope (JCMT) in the submillimeter wavelengths, with an angular resolution of $\sim 14''$ for COHRS and $\sim 15''$ for CHIMPS, respectively. The SEDIGISM survey (Structure, Excitation, and Dynamics of the Inner Galactic ISM, [Schuller et al. 2017](#)) covers 78 deg^2 in the fourth quadrant using the ^{13}CO and C^{18}O ($J=2-1$) lines at the 1 mm band. All of these CO spectral line surveys, together with other Galactic multiwavelength legacy data, will lead to significant advances in our understanding of the ISM physics of our Galaxy.

The Milky Way Imaging Scroll Painting (MWISP¹) project is an ongoing northern Galactic plane CO survey using the 13.7 m millimeter-wavelength telescope at Delingha, China (hereafter DLH telescope). The MWISP project is led by the Purple Mountain Observatory (PMO), with the full support from the staff members at Delingha. The survey observes ¹²CO, ¹³CO, and C¹⁸O ($J=1-0$) lines simultaneously for regions of $l = -10^\circ$ to $+250^\circ$ and $|b| \lesssim 5^\circ.2$ over 10 years.

In this paper, we present the results of the MWISP CO survey for regions of $l = +25^\circ.8$ to $+49^\circ.7$ and $|b| \lesssim 5^\circ.2$. Section 2 mainly describes the DLH telescope, the observing strategy and data reduction, and the details of the MWISP project. Section 3 displays the initial results for the large-scale CO maps along the Galactic plane with a large coverage in latitude. Three interesting examples, including the most distant CO arm, the bubble-like C¹⁸O structure near the HII region W40, and the vertical distribution of CO gas, are further investigated in that section. Finally, Section 4 gives a summary and future prospects.

2. THE MWISP CO SURVEY

2.1. Telescope and Multibeam Receiver System

The DLH telescope is situated at approximately ($37^\circ 22' 4N$, $97^\circ 33' 6E$), close to Delingha, the third largest city of Qinghai Province in western China. At an altitude of about 3200 m, dry and stable atmospheric conditions make Delingha an excellent site for millimeter astronomy.

The surface accuracy of the main reflector of the telescope is routinely measured and has a typical value of $\approx 73 \mu\text{m}$. The tracking accuracy of the telescope is approximately $1''-3''$ in both azimuth and elevation. The pointing accuracy for the whole sky is better than $5''$, about one-tenth of the telescope half-power beam width (HPBW) at 115 GHz ($\sim 50''$).

A 3×3 multibeam sideband-separating Superconducting Spectroscopic Array Receiver (SSAR) system (Shan et al. 2012) was installed on the DLH telescope in the 2010 winter. The centroids of the 3×3 beam patterns have a regular spacing of $172''$ (see Figure 16 in Shan et al. 2012), which are also measured before every observational season. The SSAR system employs two-sideband-separating superconductor-insulator-superconductor mixers with a typical single sideband noise temperature of 60 K and image rejection ratio above 10 dB over the frequency range of 85–115 GHz. The instrument includes Fast Fourier Transform Spectrometers (FFTSs), digital Local Oscillator (LO) sources, digital bias power supplies, and an independent intermediate frequency (IF) module.

The IF band is 2.64 ± 0.5 GHz. The ¹²CO, ¹³CO, and C¹⁸O ($J=1-0$) lines at 115.271 GHz, 110.201 GHz, and 109.782 GHz, respectively, are all within the 1 GHz band when the LO is set at 112.6 GHz. Eighteen high-resolution FFTS digital spec-

¹ <http://english.dlh.pmo.cas.cn/ic/>

trum analyzers work at 1 GHz or 200 MHz bandwidth with 16,384 channels. The 1 GHz bandwidth covers a wide velocity range for the CO line survey, while the 200 MHz bandwidth provides higher spectral resolution observations for further study (e.g., see Table 1 in Gong et al. 2018).

Typical system temperatures, which include noises from the receiver, the antenna (the optical system, the dome, and the membrane), and the atmosphere, are ~ 250 K for ^{12}CO at the upper sideband and ~ 140 K for ^{13}CO and C^{18}O at the lower sideband, respectively. Observations were calibrated using the standard chopping wheel method that allows switching between the sky and an ambient temperature load. Details on the telescope can be found at <http://www.radioast.nsd.c.cn/mwisp.php>.

2.2. Observations and Data Reduction

The sky coverage of the MWISP project is divided into 10,941 cells for the region of $l = -10^\circ$ to $+250^\circ$ and $|b| \lesssim 5^\circ$. Each cell with $30' \times 30'$ is scanned along the Galactic longitude (l) and the Galactic latitude (b) at least twice to reduce the fluctuation of noise. We chose $30' \times 30'$ as the cell's size based on three factors. One is that the cell can be completed in time with the suitable scanning parameters. This consideration is important to ensure the atmospheric stability during the 1–1.5 hr observation for a full mapping (see below). The other factor is to limit the final data size of the completed cell for one line, e.g., ~ 0.5 GB ($91 \text{ pixels} \times 91 \text{ pixels} \times 16,384 \text{ channels} \times 4 \text{ Byte}$). Finally, such a size is good to divide the whole mapping sky with a regular form, leading to the easy labeling for a cell in Galactic coordinates.

All observations are taken in position-switch On-The-Fly (OTF; see Sun et al. 2018a) mode. The scan rate is $50''$ (or $75''$) per second, with a dump time of 0.3 s (or 0.2 s), depending on a cell's elevations, off-positions, and weather conditions. The sampling interval is $15''$ ($= \text{scan rate} \times \text{dump time}$) and the spacing between scan rows is $10''$, fulfilling the oversampling of the $50''$ beam of the 13.7 m telescope. A cell thus can be fully mapped in one half an hour (or an hour) along l or b . Generally, we used the (scan rate= $50'' \text{ s}^{-1}$, dump time= 0.3 s) mode in observations. Mapping twice (or three hours) can well satisfy the expected rms noise level. The (scan rate= $75'' \text{ s}^{-1}$, dump time= 0.2 s) mode is often used for some special regions such as, for example, the low elevation cells toward $l < 10^\circ - 15^\circ$ (e.g., near the direction of the Galactic center), or some cells with far off positions (e.g., the Aquila Rift region and the Cygnus region). Sometimes, scanning twice (e.g., three hours) cannot reach the expected rms noise level, so further mapping with the (scan rate= $75'' \text{ s}^{-1}$, dump time= 0.2 s) mode is also used to reduce the rms noise for the observed cells.

The most important consideration is to maintain uniform sensitivity, which essentially depends on the weather or the total system temperature. During observations, standard sources are thus observed about every two hours in the position-switch mode. The spectral profiles and intensities of standard sources are monitored daily to check the stability of the observations.

Before observations, the off position with an area of $\sim 8' \times 8'$ (i.e., the sky coverage of the 3×3 beams) near the target cell (e.g., $\leq 2^\circ$) is carefully checked to ensure free of emission for the ^{12}CO line. However, the ^{12}CO emission in the range of 0–40 km s^{-1} is widely distributed toward the inner Galaxy, especially for the central molecular zone, the Aquila Rift, and the Cygnus region. When we observe these regions, some off-positions with a little of ^{12}CO emission ($T_{\text{MB}} \lesssim 0.3 \text{ K}$) are also used as the reference backgrounds. For these regions, ^{12}CO lines may show some weak absorption features at certain local standard of rest (LSR) velocities. The relevant information was recorded for all observed cells.

The total bandwidth of 1 GHz, with 16,384 channels, provides a channel frequency interval of 61 kHz, resulting in a velocity separation of about 0.16 km s^{-1} for ^{12}CO and 0.17 km s^{-1} for ^{13}CO and C^{18}O . A first-order (or linear) baseline was fitted for the CO spectra. Most of the bad channels in the spectra were removed. The antenna temperature, T_{A}^* , was converted to the main beam brightness temperature, T_{MB} , with the formula of $T_{\text{MB}} = T_{\text{A}}^*/(f_{\text{b}} \times \eta_{\text{MB}})$. The beam-filling factor of f_{b} is assumed to be 1 for the extended CO emission and the main beam efficiency η_{MB} varied between 40% and 50% in the past seven seasons. All intensities shown in this paper are on the T_{MB} scale.

Due to the field rotation, a larger cell size of $45'.5 \times 45'.5$ was preserved in the data processing, resulting in some overlap between neighboring cells. For each cell named as GLLL.L \pm BB.B, all CO spectra were summed together with the rms as the weight. Finally, the three-dimensional (3D) FITS data cubes of each cell were made with a grid spacing of $30''$ for ^{12}CO , ^{13}CO , and C^{18}O ($J=1-0$) lines. All data were reduced using the GILDAS software² (Pety 2005).

2.3. Characteristics and Advantages of the MWISP

The MWISP project is a large-scale, unbiased, and high-sensitivity triple CO isotope line survey for the northern Galactic plane (e.g., $l = -10^\circ$ to $+250^\circ$ and $|b| \lesssim 5^\circ.2$) that uses the 13.7 m single-dish telescope. The new nine-beam array with the OTF observation mode increases the mapping speed by roughly an order of magnitude, compared with the old single-beam system.

The DLH telescope can observe the northern Galactic plane for about 15–16 hr per day from September to April. Generally, each cell with the required rms noise (see Table 1) consumes approximately 3–5 hr (or 2–4 scans along l and b). That is, the MWISP project can map about 240–250 square degrees of the Galactic plane per year. The MWISP survey started in 2011 November and is expected to be completed in 2022.

The characteristics and advantages of the MWISP CO survey are summarized as follows:

² <http://ascl.net/1305.010> or <http://www.iram.fr/IRAMFR/GILDAS>

1. Large-scale CO mapping with a high spatial dynamic range. The MWISP project will provide us with large-scale CO maps of $\sim 2600 \text{ deg}^2$, with a moderate angular resolution of $\sim 50''$. The final full-sampling 3D CO datasets have a grid spacing of $30''$. Researchers thus can investigate the detailed structures of local MCs (e.g., 1 pixel $\lesssim 0.15 \text{ pc}$ at a distance of $\lesssim 1 \text{ kpc}$), the properties of the MCs with moderate distances (e.g., $\sim 3\text{--}6 \text{ kpc}$), and the distribution of the distant molecular gas (e.g., $\gtrsim 10 \text{ kpc}$).

2. Unbiased CO survey with high sensitivity. The unbiased survey with high sensitivity, wide velocity coverage, and high velocity resolution has a uniform sensitivity, providing us a clearer picture of the molecular gas distribution and properties of the Milky Way. Through systematic studies of the CO emission of the molecular gas, many new MCs will be revealed due to the high-quality data of the new survey, which have an rms sensitivity of ~ 0.5 (0.3) K, a velocity coverage of $\sim 2600 \text{ km s}^{-1}$, and a velocity resolution of ~ 0.16 (0.17) km s^{-1} for ^{12}CO (^{13}CO and C^{18}O) lines.

3. Simultaneous observations of ^{12}CO , ^{13}CO , and C^{18}O ($J=1\text{--}0$) transitions. The ^{12}CO emission tracing the total molecular gas can reveal structures and distributions of the diffuse gas with a typical density of 10^2 cm^{-3} . The optically thinner ^{13}CO and C^{18}O lines trace denser molecular gas with a typical density of $10^3\text{--}10^4 \text{ cm}^{-3}$ because of their less abundance with respect to H_2 and therefore less optical depth effects. Therefore, the MWISP survey is adequate for revealing the diffuse gas of MC envelopes, denser molecular gas of giant molecular clouds (GMCs), and the changes in abundance ratio between ^{13}CO and C^{18}O due to isotope-selective photodestruction of the rarer CO species.

With a spatial resolution of $\sim 50''$ and a grid spacing of $30''$, the full-sampling MWISP survey provides a rich CO data set for $b > 1^\circ$ regions, which are less covered by other CO surveys, excluding the CfA 1.2 m complete ^{12}CO ($J=1\text{--}0$) survey with a beam size of $\sim 8'$ (Dame et al. 2001). Figure 1 gives a comparison between the CfA 1.2 m CO map and our MWISP map for the Serpens/Aquila Rift MC complex. Note that the MWISP integrated map reveals more detailed structures than that of the 1.2 m CO data. Furthermore, the MWISP survey has a wider velocity coverage than that of the previous CO survey (e.g., -5 to $+135 \text{ km s}^{-1}$ for the GRS ^{13}CO survey, Jackson et al. 2006), leading to more completed velocity coverage for MCs in the first quadrant of the Milky Way (e.g., the most distant MCs beyond the solar circle).

The ongoing FUGIN survey plans to investigate the distribution and properties of molecular gas in the Galaxy with the ^{12}CO , ^{13}CO , and C^{18}O ($J=1\text{--}0$) lines (Umemoto et al. 2017). The region of $l = +10^\circ$ to $+50^\circ$ and $b = +1^\circ$ to $+1^\circ$ is fully covered using the multibeam (2×2), dual-polarization, two-sideband receiver installed in the Nobeyama 45 m telescope. Compared with the FUGIN project, the MWISP CO survey has the larger coverage (2600 deg^2 versus 160 deg^2) and the higher velocity resolution (0.16 km s^{-1} versus 0.65 km s^{-1}). Meanwhile, the sensitivity of the MWISP survey is better than that of the FUGIN project (e.g., $T_{\text{rms}}(T_{\text{MB}}) \sim 1.5 \text{ K}$

for ^{12}CO and ~ 0.7 K for $^{13}\text{CO}/\text{C}^{18}\text{O}$ at $8''.5 \times 8''.5 \times 1.3 \text{ km s}^{-1}$ in the first quadrant regions, Umemoto et al. 2017). On the other hand, the spatial resolution of the Nobeyama 45 m telescope is about 2.5 times higher than that of the DLH 13.7 m telescope. Therefore, the FUGIN data with the final grid spacing of $8''.5$ can resolve more detailed MC structures in the Galactic plane of $|b| < 1^\circ$.

In summary, the MWISP CO survey gives us a good opportunity to study the Galactic structures, the MC properties and the star formation, and the associations between the molecular gas and the extended radio sources such as, for example, H II regions and supernova remnants (SNRs). Much work has been done based on the MWISP data, such as Galactic arms traced by the CO emission (Sun et al. 2015, 2017; Du et al. 2016, 2017; Su et al. 2016), MCs and star formation (Li et al. 2013; Zhang et al. 2014b; Su et al. 2015; Zhan et al. 2016; Gong et al. 2016, 2017; Chen et al. 2016, 2017b; Xiong et al. 2017; Wang et al. 2017; Li et al. 2018b,a; Sun et al. 2018b), and interactions between SNRs and MCs (Su et al. 2014b,c, 2017a,b, 2018; Zhou et al. 2014, 2016; Chen et al. 2017a). The MWISP project also provides us an invaluable dataset for studying the distribution and kinematics of the MCs in the Milky Way (Section 3). The large-scale CO data are important in delineating the spiral structure of the Milky Way (e.g., see the recent review in Xu et al. 2018). More studies will be presented in the immediate future.

The MWISP survey is still ongoing. At the time of this writing the survey has completed about 60% of the planned 2600 square degree coverage (see the details at <http://www.radioast.nsd.c.cn/viewallobsed.php>). The complete set of the survey data generated by the MWISP project will be made publicly available via an online archive. Early access to the 3D dataset for specific regions of the sky is also possible through mutual collaboration. People who are interested in the MWISP data can request the datacube by contacting the email address dlhproposal@pmo.ac.cn. Many mosaic data cubes have already been provided to researchers through the FTP server.

3. THE SURVEY DATA

In this section, we present the CO data for the completed region of $l = +25^\circ 8$ to $+49^\circ 7$ and $|b| \lesssim 5^\circ 2$. Figure 2 shows the rms distribution of the ~ 250 square degree dataset. The typical rms noise level of the spectra is ~ 0.5 K for ^{12}CO ($J=1-0$) at a channel width of 0.16 km s^{-1} and ~ 0.3 K for ^{13}CO ($J=1-0$) and C^{18}O ($J=1-0$) at 0.17 km s^{-1} , with a spatial resolution of $\sim 50''$. Generally, the rms noise of each cell is uniform for the three CO isotope lines in the $30' \times 30'$ region. As shown in Figure 3, however, the variation in rms indeed exists between cells, e.g., $\sim 0.3-0.6$ K for ^{12}CO and $\sim 0.15-0.35$ K for $^{13}\text{CO}/\text{C}^{18}\text{O}$. Some of bright stripes with somewhat larger rms noises (e.g., $\sim 0.6-0.8$ K for ^{12}CO and $\sim 0.4-0.6$ K for $^{13}\text{CO}/\text{C}^{18}\text{O}$) also can be seen along l and b , with lengths of several tens of arcminutes. These features are due to the bad weather (or the large system temperature) in the OTF scanning. Table 1 lists the parameters of the CO data used in this paper.

The distributions of the CO emission are shown through intensity maps, intensity-weighted mean velocity maps, and position–velocity (PV) diagrams. Some interesting results of the new CO survey are also investigated. The CO data are smoothed to the 0.5 km s^{-1} velocity resolution in order to improve the sensitivity for weak emission. The improved rms levels of the analyzed data are of $\sim 0.28 \text{ K}$ for the ^{12}CO line and $\sim 0.16 \text{ K}$ for the ^{13}CO and C^{18}O lines, respectively.

3.1. CO gas with $V_{\text{LSR}} < 0 \text{ km s}^{-1}$

Very recently, [Su et al. \(2016\)](#) and [Sun et al. \(2017\)](#) presented the results of distant MCs traced by CO emission between $l = 34.75^\circ$ and $l = 45.25^\circ$. These MCs with negative velocities are divided into the distant Outer Arm and the Extreme Outer Galaxy (EOG), respectively. These two parts of the molecular gas are very likely the extension of the Norma–Cygnus Arm and the Scutum–Centaurus Arm in the first quadrant (i.e., molecular gas structures from the fourth quadrant of the inner Galaxy to the first quadrant of the outer Galaxy). Actually, the more negative velocity feature at $V_{\text{LSR}} < 0 \text{ km s}^{-1}$ was proposed to be from the Outer Scutum-Centaurus Arm ([Dame & Thaddeus 2011](#)).

With the progress of the MWISP project, larger mapping was completed for the range of $+25.8^\circ \lesssim l \lesssim +49.7^\circ$ and $|b| \lesssim 5.2^\circ$. Figure 4 shows the spatial distribution of the CO gas with $V_{\text{LSR}} < 0 \text{ km s}^{-1}$, together with the corresponding LSR velocity information. A large amount of new ^{12}CO emission is revealed because of the high sensitivity and the large coverage of the unbiased survey. Some of the MCs with relatively strong ^{12}CO emission have the corresponding ^{13}CO emission, but none of them show significant C^{18}O emission under the improved rms level of $\sim 0.16 \text{ K}$ at the smoothed velocity resolution of 0.5 km s^{-1} . Higher resolution and sensitivity observations are expected to detect the weak emission of the dense gas far away from us.

Some of MCs with $V_{\text{LSR}} \lesssim 0 \text{ km s}^{-1}$ are likely the local molecular gas due to their $\sim 0 \text{ km s}^{-1}$ LSR velocities and relatively high $|b|$ values (e.g., $|b| \gtrsim 2.5^\circ$; see the Aquila Rift region near $l \sim 26^\circ - 32^\circ$ in the lower panel of Figure 4). However, most of $V_{\text{LSR}} < 0 \text{ km s}^{-1}$ MCs in Figure 4 are believed to lie beyond the solar circle. Obviously, CO emission is mainly concentrated near the Galactic plane, excluding the possible local gas in the Aquila Rift region at high $|b|$. In spite of this, the distant CO gas seems to also be slightly displaced from $b = 0^\circ$, which was explained by the warped plane at larger Galactocentric distances and the apparent tilted structure caused by the Sun’s z -height above the physical midplane of the Galactic disk (see [Su et al. 2016](#); [Sun et al. 2017](#)).

Due to the large distances, many MCs have small angular sizes and weak CO emission. These MCs are relatively isolated in l - b - v space. Despite these properties, some interesting distant MCs with brighter CO emission also display extended concentrations, which usually have special morphologies such as filaments, arcs/shells, and

irregular cavity-like structures. These extended concentrations could be related to the massive star-forming activities in the surroundings. Very recently, [Wenger et al. \(2018\)](#) investigated the CO properties toward star-forming regions in the the Outer Scutum-Centaurus Arm using single pointing observation of the 12 m telescope located at Arizona Radio Observatory. Benefiting from the full CO map and the high sensitivity of the MWISP data, we will systematically study the relationship between the distant MCs and the surrounding star formation activities. Detailed identification and analyses of these MCs will be presented in future papers. Section 3.3.1 shows some initial results for the CO gas at the edge of the Galaxy.

3.2. CO gas with $V_{\text{LSR}} > 0 \text{ km s}^{-1}$

Figure 5 shows the ^{13}CO ($J=1-0$) intensity map in the $0-130 \text{ km s}^{-1}$ interval, overlaid with radio continuum contours from the Effelsberg 11 cm survey ([Reich et al. 1990](#)). Some bright and/or extended radio sources discussed below are labeled on the guide map.

Figures 6 and 7 show ^{12}CO and ^{13}CO channel maps, respectively. The channel maps are made by integrating emission over a 10 km s^{-1} velocity bin from 0 km s^{-1} to 120 km s^{-1} . The $120-130 \text{ km s}^{-1}$ ^{12}CO and ^{13}CO gas, which displays emission only near $l \sim 26^\circ - 31^\circ$, is presented in Figure 8. A large number of MC structures and features are seen in both of the ^{12}CO and ^{13}CO channel maps.

For the $0-20 \text{ km s}^{-1}$ maps, the most prominent features are the Aquila Rift (e.g., see Figure 3 in [Dame & Thaddeus 1985](#)), which displays large-scale, diffuse, and enhanced CO emission in the field of view (FOV). The MWISP survey, with the wide spatial dynamic range, reveals lots of detailed structures for the large-scale molecular gas not far from us (i.e., $d \lesssim 450 \text{ pc}$; [Ortiz-León et al. 2017](#)). Large-scale extended structures are also discernible from the PV diagrams of ^{12}CO and ^{13}CO emission (see the region of $V_{\text{LSR}} \sim 0-20 \text{ km s}^{-1}$ and $l \sim 26^\circ-40^\circ$ in Figure 9). The ^{12}CO $J=2-1$ and ^{13}CO $J=2-1$ emission from the Aquila Rift region was investigated by [Nakamura et al. \(2017\)](#) using the 1.85 m telescope. Combinations of our CO $J=1-0$ data and the 1.85 m CO $J=2-1$ data will help us understand the detailed molecular gas properties of such local regions.

Many of bright CO concentrations in the velocity interval of $\sim 0-30 \text{ km s}^{-1}$ are found to be near the Galactic plane of $b \sim -0.4$ to $+0.6$, excluding the diffuse and extended emission from the local MCs (e.g., the Aquila Rift region discussed above). These concentrations, which have typical angular sizes of several arcminutes, are likely related to the distant Perseus Arm in the first quadrant of the Galaxy.

For $20-40 \text{ km s}^{-1}$ gas, the ^{12}CO and ^{13}CO emission is found to be extended over a large region from $l \sim 34^\circ - 44^\circ$ and $|b| \lesssim 5^\circ$ in the channel maps. This GMC complex is less studied in the literature. A 170 pc long giant molecular filament (GMF) of G40.82-1.41, which is at $\sim 2 \text{ kpc}$ (e.g., the kinematic distance and the extinction distance, [Su et al. 2018](#)), is probably a part of the GMC complex. The extended

molecular gas at $b \gtrsim 0^\circ$ of the GMC is related to the H II regions Sh 2-75 (at $l = 40^\circ 12$, $b = 1^\circ 50$) and Sh 2-76 (at $l = 40^\circ 44$, $b = 2^\circ 45$). One of the H II regions, Sh 2-76, is exactly located at a distance of $1.92^{+0.09}_{-0.08}$ kpc from the parallax measurements of 0.521 ± 0.024 mas (Chibueze et al. 2017).

At $30\text{--}60 \text{ km s}^{-1}$, significant CO emission appears at $l \sim 34^\circ\text{--}36^\circ$ and $b \sim -3^\circ$ to $+1^\circ$, which is roughly perpendicular to the Galactic plane. Enhanced CO emission in the GMC complex displays complicated morphologies, such as multi-shells, bubbles, and cometary bright-rimmed structures. The GMC complex is associated with the high-mass star-forming region W48 (G35.2–1.8) at a parallax distance of $3.27^{+0.56}_{-0.42}$ kpc (Zhang et al. 2009). The very bright SNR G34.7–0.4, also known as W44 at a near kinematic distance of ~ 3.3 kpc (e.g., Su et al. 2014a), may be associated with the GMC complex.

For the $V_{\text{LSR}} \gtrsim 50 \text{ km s}^{-1}$ molecular gas, CO emission is mainly confined within $|b| \lesssim 1^\circ$. In addition to the CO emission close to the Galactic plane, considerable MCs are detected in $1^\circ \lesssim |b| \lesssim 2^\circ$, even for velocities near the tangent point (see $80\text{--}120 \text{ km s}^{-1}$ maps in Figures 6 and 7). These features have not been revealed by previous CO surveys (e.g., FCRAO GRS project, Jackson et al. 2006) due to the limited Galactic latitude coverage of $|b| \lesssim 1^\circ$ toward the first quadrant of the Milky Way. From Figure 9, we find that the PV diagram of the MWISP ^{13}CO data is consistent with the previous PV map of the GRS ^{13}CO survey (see Figure 3 in Jackson et al. 2006). Furthermore, some new features in the ^{13}CO PV diagram are unveiled for the $V_{\text{LSR}} \lesssim 50 \text{ km s}^{-1}$ range (e.g., see structures at $l \sim 38^\circ\text{--}42^\circ$ and $V_{\text{LSR}} \sim 25\text{--}45 \text{ km s}^{-1}$, the rectangle in the diagram) because of the larger latitude coverage of the MWISP survey. The CO emission of the structure is from the molecular gas associated with H II regions Sh 2-75 and Sh 2-76.

Figure 10 displays the spatial and velocity distribution of the C^{18}O ($J=1\text{--}0$) emission in the velocity range of $0\text{--}40 \text{ km s}^{-1}$. Enhanced C^{18}O emission is clearly seen near $l \sim 28^\circ 7$ and $b \sim 3^\circ 7$, which is probably associated with the feedback of massive stars in the Serpens south and the W40 complex (see Section 3.3.2). Excluding C^{18}O emission from the local MCs such as the Aquila Rift, the rest of C^{18}O gas is mainly confined in $b \sim -2^\circ$ to $b \sim 3^\circ$. In the figure, two other prominent C^{18}O features, which are located at $l \sim 35^\circ$ and $l \sim 40^\circ$, are found to be away from the $b = 0^\circ$ plane. The two C^{18}O features are related to the massive star-forming region W48 and H II regions Sh 2-75 and Sh 2-76, respectively.

Figure 11 shows the C^{18}O emission in the velocity interval of $40\text{--}80 \text{ km s}^{-1}$ and $80\text{--}120 \text{ km s}^{-1}$, which is mainly within $|b| \lesssim 2^\circ$ and $|b| \lesssim 1^\circ$, respectively. For the $40\text{--}80 \text{ km s}^{-1}$ maps, the W48 GMC complex at $l \sim 35^\circ$, which is roughly perpendicular to the $b = 0^\circ$ plane, is clearly seen in Figures 11a and 11b. On the other hand, the W51 GMC complex at a distance of $5.41^{+0.31}_{-0.28}$ kpc (e.g., the trigonometric parallax from Sato et al. 2010) also can be seen at $l \sim 49^\circ$. The massive star-forming region W51 was recently reviewed by Ginsburg (2017, and references therein).

For the $V_{\text{LSR}} = 80\text{--}120 \text{ km s}^{-1}$ maps (see Figures 11c,d), the most enhanced C^{18}O emission with $\sim 10 \text{ K km s}^{-1}$ is associated with the mini-starburst region W43 at ($l \sim 30^\circ 7$, $b \sim 0^\circ 0$). The massive star-forming region, which is at a parallax distance of $5.49_{-0.34}^{+0.39}$ kpc (Zhang et al. 2014a), is probably at or close to the near end of the Galactic long bar. The ongoing star-forming activity of the global mini-starburst region is likely the result of the massive gas clouds accumulated by the bar potentials and kinematics. The gas property of the interesting GMC complex W43 was studied by many groups (e.g., Nguyen Luong et al. 2011; Carlhoff et al. 2013; Motte et al. 2014; Sofue et al. 2018).

For the survey data presented here, the C^{18}O emission is relatively discrete in comparison with the extended ^{12}CO and ^{13}CO emission. Researchers thus can identify the main structures of MCs using C^{18}O emission due to the less velocity crowding and line blending (e.g., see the W40 region in Section 3.3.2).

As shown in Figure 11, the distribution of the C^{18}O emission is below the plane of $b = 0^\circ$, especially for the $40\text{--}80 \text{ km s}^{-1}$ MCs. Near the tangent point, where the dense gas is more concentrated in the plane, the dominant part of them is also below the plane (e.g., the $80\text{--}120 \text{ km s}^{-1}$ maps). This interesting feature is explained by the Sun’s offset above the physical midplane of the Milky Way (e.g., $z_{\text{Sun}} \sim 17.1 \text{ pc}$; see discussions and Figure 7 in Su et al. 2016). We further investigate the phenomena using MC samples close to the tangent point, e.g., the CO gas with $V_{\text{LSR}} > 60 \text{ km s}^{-1}$ (Section 3.3.3).

3.3. Interesting Examples

3.3.1. CO gas at the Edge of the Milky Way

The CO emission of the distant molecular gas is very weak. Due to the warping and flaring of the outer gas disk, the distant MCs with negative velocities are concentrated at the somewhat higher latitudes, which is different from the molecular gas in the first quadrant of the inner Galaxy. The unbiased MWISP CO survey has a wide velocity and areal coverage, meanwhile there is also a high sensitivity, allowing us to systematically investigate weak CO emission far away from the Sun (see Figure 4). Compared with the CfA 1.2 m CO survey (Dame et al. 2001), the MWISP CO data from the 13.7 m telescope obviously reveal detailed distributions and structures of the distant MCs.

Figure 12 shows the longitude–velocity (l – v) diagram of the ^{12}CO emission for the $V_{\text{LSR}} \lesssim 0 \text{ km s}^{-1}$ molecular gas. Note that the CO intensity is multiplied by a factor of 100 for the corresponding signal velocity range but not the whole velocity range. The noise is therefore suppressed and the tiny features of weak CO emission are enhanced in the l – v diagram. Based on the diagram, we find that the bright emission (thick blue parts in the figure) exhibits a large-scale molecular gas structure outside the solar circle. On a large scale, the structure shows a velocity gradient of $\sim 2.5\text{--}3.0 \text{ km s}^{-1}\text{degree}^{-1}$ and has relatively enhanced ^{12}CO emission, which is likely

from MCs within the Outer Arm (or the Norma–Cygnus Arm) in the first quadrant. Moreover, the large-scale structure is comprised of several interesting substructures in the l – v space, which themselves are worthy of further investigation.

In addition to the enhanced ^{12}CO emission, considerable molecular gas with weaker CO emission at more negative LSR velocities is also discerned from Figure 12 (see the regions between the red lines, i.e., $V_{\text{LSR}} = -1.57 \times l + 4.34 \pm 12 \text{ km s}^{-1}$). The most negative velocity is at $\sim -75 \text{ km s}^{-1}$ with low surface brightness. These MCs are probably in a distant section of the Scutum–Centaurus Arm (designated as the OSC by Dame & Thaddeus 2011), which is referred to as the EOG region by Sun et al. (2017). The trend of the molecular gas in the l – v space is approximately described by a linear fit of $V_{\text{LSR}} = -1.57 \times l + 4.34 \text{ km s}^{-1}$, which is in good agreement with previous studies (see Dame & Thaddeus 2011; Sun et al. 2017). The velocity gradient of $\sim 1.6 \text{ km s}^{-1} \text{ degree}^{-1}$ for the EOG gas is smaller than that of the molecular gas of the Outer Arm in the l – v space (e.g., $\sim 2.8 \text{ km s}^{-1} \text{ degree}^{-1}$ in Su et al. 2016). The uncertainty of the tentative fit is largely due to the limited longitude coverage. On the other hand, the OSC Arm may consist of several broken lines with somewhat different slopes in the l – v space. Further MWISP data from $l = 0^\circ$ to 26° and $l = 50^\circ$ to 100° can give us a firmer conclusion (e.g., see Figure 3 in Sun et al. 2015).

Figure 13 displays the distribution of the EOG ^{12}CO emission. Samples in the figure are selected from the MCs with $V_{\text{LSR}} \lesssim -1.57 \times l + 4.34 \text{ km s}^{-1}$, which reduces possible contamination from the Outer Arm gas. We find that these most distant MCs are quite sparse in the l – b space and indeed located above the $b = 0^\circ$ plane. For regions of $l \sim 40^\circ$ – 50° , the lack of the EOG CO emission in the map indicates that the slope of -1.57 in our fitting is probably too steep for the distant MCs at larger longitudes (e.g., a slightly flat slope of $\gtrsim -1.4$ for $l \gtrsim 40^\circ$ CO gas in the l – v space). Two intensity peaks are located at $b \sim 1^\circ.2$ and $b \sim 2^\circ.8$, or $\sim 370 \text{ pc}$ and $\sim 870 \text{ pc}$ above the $b = 0^\circ$ plane, assuming a median heliocentric distance of 17.8 kpc (Sun et al. 2017). These values are several times larger than that of the Outer Arm gas (e.g., $0^\circ.42$ or $\sim 110 \text{ pc}$ at a heliocentric distance of 15 kpc ; Su et al. 2016), indicating the different distributions of the two MC groups for the distant $V_{\text{LSR}} < 0 \text{ km s}^{-1}$ gas. Indeed, the more negative the value of the LSR velocity is, the higher the Galactic latitude of the distant molecular gas.

3.3.2. Bubble-like C^{18}O Structure near the HII region W40

At similar distances, there may be multiple MCs with different velocity fields in the ISM, leading to complicated molecular gas structures. Simultaneous ^{12}CO , ^{13}CO , and C^{18}O ($J=1-0$) line observations can provide a more complete picture of the molecular gas properties, such as structures, kinematics, and dynamics. Star formation is associated with molecular gas. The MWISP survey is helpful for studying the relationship between MCs and star-forming activity in the Milky Way.

An intriguing case is the W40 region, which is part of the Serpens/Aquila Rift MC complex. The region is located at a distance of $436.0 \pm 9.2 \text{ pc}$ according to the mea-

measurements of proper motions of seven stars across the MC complex (Ortiz-León et al. 2017). Nakamura et al. (2017) covered the MC complex using ^{12}CO , ^{13}CO , and C^{18}O ($J=2-1$) lines with the 1.85 m telescope. The gas toward W40 within an area of ~ 1 square degree was further investigated by the Nobeyama 45 m telescope (Shimoikura et al. 2018). Based on the MWISP survey on the 13.7 m telescope, a prominent bubble-like structure is unveiled in the C^{18}O intensity map (e.g., see the upper right corner of Figure 10).

Figure 14 displays the close-up view toward the W40 region, where the blue, green, and red colors represent the ^{12}CO , ^{13}CO , and C^{18}O emission, respectively. The circular morphology of the dense gas in the three-color image is centered at ($l = 29^\circ 07'$, $b = 3^\circ 82'$), with a radius of $0^\circ 45'$. Obviously, the emission of the dense gas traced by ^{13}CO and C^{18}O lines is mainly concentrated in the western half of the bubble-like structure, while the C^{18}O structure in the eastern half is broken. The LSR velocity of C^{18}O emission peaks at $V_{\text{LSR}} \sim 7.5 \text{ km s}^{-1}$ on the bubble-like structure, where both the ^{12}CO and ^{13}CO lines show the striking self-absorption features (see the typical spectra to the right of the figure).

The strongest ^{12}CO emission of $T_{\text{MB}} \sim 37 \text{ K}$ at $V_{\text{LSR}} \sim 4.5 \text{ km s}^{-1}$ is located at ($l = 28^\circ 75'$, $b = 3^\circ 51'$), which is close to the center of the H II region W40 (see the purple circle in Figure 14). The typical peak temperature of the optically thick ^{12}CO line is nearly 10 K in some bright regions, while considerable ^{12}CO emission has a lower peak temperature of $\sim 4-6 \text{ K}$ in other faint regions. Huge regions of molecular gas with relatively weak CO emission extend several tens of square degrees over the FOV (e.g., see $0-10 \text{ km s}^{-1}$ and $10-20 \text{ km s}^{-1}$ maps in Figure 6).

Figure 15 displays the gas distribution in velocity intervals of 3–5, 5–7, 7–9, and 9–11 km s^{-1} toward the complex. For the 3–5 km s^{-1} gas, the very strong CO emission is found to surround the W40 H II region (the 9' purple circle in the map), while CO emission seems to be lacking toward the center of the H II region. The enhanced dense gas, which is represented by the bright CO emission, exhibits a bubble-like structure in the 5–7 and 7–9 km s^{-1} maps. We use a large circle with a diameter of $0^\circ 9'$ to show the bubble-like structure.

In the northeastern region of the broken C^{18}O bubble-like structure (i.e., near $l \sim 29^\circ 5'$ and $b \sim 4^\circ 0'$), several finger-like protrusions traced by ^{12}CO and ^{13}CO emission are found to point to the W40 H II region (see the $V_{\text{LSR}} \sim 9-11 \text{ km s}^{-1}$ map in Figure 15). Moreover, the CO data reveal many interesting features, including rim-bright MCs, molecular gas bubbles/cavities, and shells/arcs in the complicated region. These features may be related to the strong feedback from the H II region W40.

Figure 16 exhibits the velocity distribution of the C^{18}O gas toward the W40 region. Three main velocity components are recognized, such as the partial shell structure surrounding W40 at $V_{\text{LSR}} \sim 5-6 \text{ km s}^{-1}$ (thick blue), the western half bubble-like structure at $V_{\text{LSR}} \sim 7-8 \text{ km s}^{-1}$ (thin blue to green), and the eastern broken bubble-

like structure at $V_{\text{LSR}} \sim 9 \text{ km s}^{-1}$ (red). Some line-broadening features of ^{12}CO gas (e.g., $V_{\text{LSR}} \lesssim 2 \text{ km s}^{-1}$ and $V_{\text{LSR}} \sim 12 \text{ km s}^{-1}$) are also revealed in the whole region, indicating the potential outflow candidates. Detailed analysis of the nearby region will be helpful for understanding the relationship between the molecular gas and the ongoing star formation.

3.3.3. CO gas distribution perpendicular to the Galactic plane

Dame & Thaddeus (1994) suggested that a thick molecular disk traced by faint CO emission is well above the central thin CO disk in the inner Galaxy. Their results are based on CO observations of the 1.2 m telescope for narrow regions of Galactic longitudes $l = 30^\circ, 40^\circ,$ and 50° and Galactic latitudes $|b| < 4^\circ$. Benefiting from the unbiased, high-sensitivity, and large-area MWISP CO survey, we have a pretty good chance of studying the second, faint, and thick disk component of the molecular gas toward the inner Galaxy.

Channel maps of ^{12}CO and ^{13}CO (Figures 6 and 7) show that there are many MCs near the terminal velocity extending up to $\sim 1^\circ\text{--}3^\circ$ from the plane. Some MCs have extremely b values of $> 4^\circ$. These MCs at $|b| \gtrsim 1^\circ$ and $V_{\text{LSR}} \geq 60 \text{ km s}^{-1}$ are relatively isolated with respect to the molecular gas near the Galactic plane. The MCs with weak CO emission, which are often associated with the enhanced HI emission (e.g., to compare with the GALFA data, Peek et al. 2011), have little velocity crowding at regions of relatively high b .

Peak ^{12}CO velocities of $V_{\text{LSR}} \geq 60 \text{ km s}^{-1}$ molecular gas are extracted pixel by pixel for the whole region of $+25.8 \lesssim l \lesssim +49.7$ and $|b| \lesssim 5.2$. The pixels with three consecutive channels $\geq 3 \times \text{rms}$ (or $\sim 0.8 \text{ K}$ for the smoothed velocity resolution of 0.5 km s^{-1}) would be considered to be the valid signal. The near kinematic distances of the CO signal are calculated assuming the flat Galactic rotation curve model (e.g., Reid et al. 2014). Then, the distances from the $b = 0^\circ$ plane (i.e., z) are estimated for each pixel. To reduce sample fluctuations, z values are combined every 10 pc per bin from -500 pc to $+400 \text{ pc}$. CO intensities are averaged for all valid CO signal per bin. The error bars are estimated from the express of $I_{\text{mean}}(\text{CO})/(\text{number of pixels per bin})^{0.5}$. As a consequence, the error bars of the high- z samples are obviously larger than those of points near the Galactic plane.

Figure 17 displays the vertical distribution of the CO gas. We find that one Gaussian model produces a poor fit to the histogram of the CO distribution from the Galactic plane (e.g., $\chi^2/\text{dof}=94.8/86$). The full width at half maximum (FWHM) of the one Gaussian component is 162.7 pc, which is larger than results from other studies (e.g., FWHM $\sim 90\text{--}110 \text{ pc}$ for the inner Galaxy, e.g., Malhotra 1994b; Nakanishi & Sofue 2006, 2016; Heyer & Dame 2015; Roman-Duval et al. 2016). Moreover, the mean emission peak at $z \sim -11 \text{ pc}$ and the prominent broad wing at $|z| \gtrsim 100 \text{ pc}$ cannot be fitted by the one Gaussian model.

On the contrary, the model of two Gaussian components works better ($\chi^2/\text{dof}=60.5/84$, also see the red-thick line in Figure 17). Table 2 shows the pa-

rameters of the best fit. The best fit of the zero-point is at $\sim 3.8 \text{ K km s}^{-1}$, which is roughly 5σ of the CO integrated intensity. The value of the zero-point depends on the current rms level of the MWISP survey, in which samples with three consecutive channels greater than $3\times$ rms ($\sim 0.8 \text{ K}$) are chosen as the valid ^{12}CO signal of the MCs. A few points near the zero-point are from the noise (e.g., bad channels and baseline fluctuations in the velocity axis of the 3D data cubes). These bad points, which are randomly distributed in the area, are readily discerned by checking their spectra.

Samples away from the Galactic plane with values above 3.8 K km s^{-1} are actually from the high- z CO emission. An example is the unusual peak at $z \sim -435 \text{ pc}$ (Figure 17). CO emission of this feature is mostly from MC G40.331–4.302 at $V_{\text{LSR}} \sim 77\text{--}84 \text{ km s}^{-1}$. The high $|b|$ MC is associated with the W50 nebula, which has a near kinematic distance of 4.9 kpc, as estimated from the large-scale gas at $V_{\text{LSR}} = 77 \text{ km s}^{-1}$ (see the detailed HI and CO analysis in Su et al. 2018). At the distance of 4.9 kpc, the true displacement from the $b = 0^\circ$ plane is $z \approx -370 \text{ pc}$ for the $b = -4^\circ.302$ molecular gas, which is likely related to the energetic jets of the microquasar SS 433 in W50 (i.e., jet–ISM interactions discussed in Su et al. 2018).

The two Gaussian components correspond to the central thin molecular gas disk (FWHM=88.5 pc) and the extended thick CO disk (FWHM=276.8 pc), respectively. The thickness ratio of the two Gaussian components is $\text{FWHM}(\text{Thick plane})/\text{FWHM}(\text{Thin plane}) \sim 3.1$ for the region of Galactocentric distances of $R_{\text{GC}} \sim 3.9\text{--}6.4 \text{ kpc}$ (mean at $\sim 5.4 \text{ kpc}$ for all samples) toward the inner Galaxy. These results are consistent with previous studies (Dame & Thaddeus 1994; Malhotra 1994a). The total intensity ratio between $|z| \gtrsim 100 \text{ pc}$ and $|z| \lesssim 100 \text{ pc}$ is about 0.03, indicating very faint CO emission for the second (or thick) molecular gas component.

In the above calculation, we used the A5 rotation curve model of Reid et al. (2014), in which the values of $R_0=8.34 \text{ kpc}$ and $V_0=240 \text{ km s}^{-1}$ are adopted. The thickness of the molecular gas disk will increase by a factor of ~ 1.1 for the parameters of $R_0=8.5 \text{ kpc}$ and $V_0=220 \text{ km s}^{-1}$.

We have shown that CO emission in the first quadrant of the inner Galaxy is somewhat below the Galactic plane based on channel maps in Figure 6. Further quantitative analysis indicates that the distribution of molecular gas is actually below the $b = 0^\circ$ plane for the $V_{\text{LSR}} \gtrsim 60 \text{ km s}^{-1}$ CO emission (Figure 17 and Table 2). Assuming that the inner disk of our Galaxy is flat and tilted, we derive the Sun’s offset from the Galactic physical midplane based on the molecular gas distribution along the Galactic latitude. Considering $\frac{z_{\text{Sun}}}{R_0} \approx \frac{z_{\text{peak}}}{R_{\text{GC}}(\text{mean})}$, the Sun is about $8.34 \times \frac{11.3}{5.4} \approx 17.5 \text{ pc}$ above the physical midplane of the Milky Way, which agrees well with our previous study of $\sim 17.1 \text{ pc}$ (Su et al. 2016).

4. SUMMARY AND FUTURE PROSPECTS

The MWISP project is a large, systematic, and unbiased CO survey of the northern Galactic plane using the 13.7 m millimeter-wavelength telescope with a 3×3 beam array. As part of the legacy survey, the ~ 250 deg² regions of the first quadrant of $l = +25^\circ.8$ to $+49^\circ.7$ and $|b| \lesssim 5^\circ.2$ are completely mapped during the period of 2011–2018 in the ^{12}CO , ^{13}CO , and C^{18}O ($J=1-0$) lines. Using the OTF mode, we achieved the high-quality CO data with an angular resolution of $\sim 50''$ and grid sampling of $30''$. The rms noise level of the data is ~ 0.5 K for ^{12}CO at a channel width of 0.16 km s⁻¹ and ~ 0.3 K for ^{13}CO and C^{18}O at 0.17 km s⁻¹.

Using the new CO data, we investigate the distant molecular gas in the first quadrant of the Milky Way. The ^{12}CO distribution of the most distant gas, which is weak and isolated in space and velocity, is described by the equation of $V_{\text{LSR}} \lesssim -1.57 \times l + 4.34$ km s⁻¹. We believe that these MCs are from the Scutum–Centaurus Arm in the outer Galaxy, which are mainly concentrated in $b \gtrsim 0^\circ$ regions of the first quadrant of the Milky Way due to the warping of the Galactic outer disk.

A bubble-like structure with a diameter of $0^\circ.9$ in C^{18}O emission is revealed toward the Serpens/Aquila Rift MC complex. We suggest that the interesting structure, together with the surrounding rim-bright MCs and molecular shells/arcs, may be related to the nearby H II region W40, which is just located at the southwestern edge of the bubble-like dense gas structure.

In addition to a thin CO disk with an FWHM of ~ 88.5 pc, another faint and thick molecular gas disk with an FWHM of ~ 276.8 pc is confirmed based on the high-quality CO data. The thickness (or FWHM) of the faint CO component, which is about 3.1 times as wide as the thin CO layer, is roughly comparable with the H I thickness for regions of $R_{\text{GC}} \sim 4-6$ kpc (FWHM $\sim 250-300$ pc in [Dickey & Lockman 1990](#); [Lockman & Gehman 1991](#); [Nakanishi & Sofue 2016](#)). The second component of the faint CO gas is probably related to the activity of massive stars near the Galactic plane, which needs to be further explored. The Sun’s offset is found to be ~ 17.5 pc above the Galactic disk, according to the CO intensity peak at $z_0 = -11.3$ pc.

As shown by the examples in the paper, the unbiased MWISP CO survey is powerful for studying the distribution and properties of the molecular gas, the Galactic structures traced by MCs, and the relationship between molecular gas and star formation. According to the guide map of [Figure 5](#), we exhibit that the molecular gas is tightly correlated with the radio emission. The bright radio emission is thought to be from the stellar feedback, such as H II regions and SNRs, which have profound effects on their surrounding ISM. Therefore, the large-scale CO survey with high dynamic range is also an excellent dataset for studying the effects of stellar feedback on MCs (i.e., outflows, H II regions, stellar winds, and SNRs on the surrounding molecular gas environment).

Further MC identification is important for the extended CO emission with velocity crowding. New methods, such as SCIMES (i.e., Spectral Clustering for Interstellar Molecular Emission Segmentation, [Colombo et al. 2015](#)), may be useful for

defining the structures of the diffuse CO emission and assessing the global properties of the MCs. [Miville-Deschênes et al. \(2017\)](#) recently investigated the properties of 8107 Galactic MCs using a hierarchical cluster identification applied to the result of a Gaussian decomposition of the CfA 1.2 m CO data. On the other hand, [Roman-Duval et al. \(2016\)](#) examined the spatial distribution of the diffuse gas traced by ^{12}CO emission and the dense gas traced by ^{13}CO and CS emission in the inner Galaxy. Based on CO data of multiple surveys, they showed that CO emission is very important for studying the dense star-forming MCs and the diffuse molecular ISM in the Galaxy.

Using the ^{12}CO , ^{13}CO , and C^{18}O ($J=1-0$) lines in combination with the wide velocity coverage, the high-velocity resolution, and the large-scale mapping provided by the MWISP, we can separate distinct clouds at similar velocities, investigate detailed kinematic information of the molecular gas at complicated regions, and provide the MC catalog traced by CO emission. More sophisticated methods will be explored to systematically analyze the spatial and kinematic features of MCs in the Milky Way based on the new CO survey.

We gratefully acknowledge the staff members of the Qinghai Radio Observing Station at Delingha for their support of the observations. We thank the anonymous referee for a careful reading of the manuscript and several critical suggestions that improved the paper. This work is funded by the National Key R&D Program of China through grants 2017YFA0402701 and 2017YFA0402702. J.Y. acknowledges CAS support through grant QYZDJ-SSW-SLH047. X.C. acknowledges support by the NSFC through grant 11473069. Y.S. was supported by the NSFC through grant 11773077.

Facility: PMO 13.7m

Software: GILDAS/CLASS ([Pety 2005](#))

REFERENCES

- Barnes, P. J., Muller, E., Indermuehle, B., et al. 2015, *ApJ*, 812, 6
- Bolatto, A. D., Wolfire, M., & Leroy, A. K. 2013, *ARA&A*, 51, 207
- Burton, M. G., Braiding, C., Glueck, C., et al. 2013, *PASA*, 30, e044
- Carlhoff, P., Nguyen Luong, Q., Schilke, P., et al. 2013, *A&A*, 560, A24
- Chen, X., Xiong, F., & Yang, J. 2017a, *A&A*, 604, A13
- Chen, Z., Jiang, Z., Tamura, M., Kwon, J., & Roman-Lopes, A. 2017b, *ApJ*, 838, 80
- Chen, Z., Zhang, S., Zhang, M., et al. 2016, *ApJ*, 822, 114
- Chibueze, J. O., Hamabata, H., Nagayama, T., et al. 2017, *MNRAS*, 466, 4530
- Colombo, D., Rosolowsky, E., Ginsburg, A., Duarte-Cabral, A., & Hughes, A. 2015, *MNRAS*, 454, 2067
- Combes, F. 1991, *ARA&A*, 29, 195
- Dame, T. M., Hartmann, D., & Thaddeus, P. 2001, *ApJ*, 547, 792
- Dame, T. M., & Thaddeus, P. 1985, *ApJ*, 297, 751

- . 1994, *ApJL*, 436, L173
- . 2011, *ApJL*, 734, L24
- Dempsey, J. T., Thomas, H. S., & Currie, M. J. 2013, *ApJS*, 209, 8
- Dickey, J. M., & Lockman, F. J. 1990, *ARA&A*, 28, 215
- Du, X., Xu, Y., Yang, J., & Sun, Y. 2017, *ApJS*, 229, 24
- Du, X., Xu, Y., Yang, J., et al. 2016, *ApJS*, 224, 7
- Ginsburg, A. 2017, *Star Formation Newsletter* 290, arXiv:1702.06627
- Gong, Y., Li, G. X., Mao, R. Q., et al. 2018, *A&A*, 620, A62
- Gong, Y., Mao, R. Q., Fang, M., et al. 2016, *A&A*, 588, A104
- Gong, Y., Fang, M., Mao, R., et al. 2017, *ApJL*, 835, L14
- Heyer, M., & Dame, T. M. 2015, *ARA&A*, 53, 583
- Heyer, M. H., Brunt, C., Snell, R. L., et al. 1998, *ApJS*, 115, 241
- Jackson, J. M., Rathborne, J. M., Shah, R. Y., et al. 2006, *ApJS*, 163, 145
- Lee, Y., Stark, A. A., Kim, H.-G., & Moon, D.-S. 2001, *ApJS*, 136, 137
- Li, C., Wang, H., Zhang, M., et al. 2018a, *ApJS*, 238, 10
- Li, J.-Y., Jiang, Z.-B., Liu, Y., & Wang, Y. 2013, *RAA*, 13, 921
- Li, Y., Li, F.-C., Xu, Y., et al. 2018b, *ApJS*, 235, 15
- Lockman, F. J., & Gehman, C. S. 1991, *ApJ*, 382, 182
- Malhotra, S. 1994a, *ApJ*, 437, 194
- . 1994b, *ApJ*, 433, 687
- Miville-Deschênes, M.-A., Murray, N., & Lee, E. J. 2017, *ApJ*, 834, 57
- Mizuno, A., & Fukui, Y. 2004, in *ASP Conf. Ser.*, Vol. 317, *Milky Way Surveys: The Structure and Evolution of our Galaxy*, ed. D. Clemens, R. Shah, & T. Brainerd, (San Francisco, CA: ASP), 59
- Motte, F., Nguyễn Luong, Q., Schneider, N., et al. 2014, *A&A*, 571, A32
- Nakamura, F., Dobashi, K., Shimoikura, T., Tanaka, T., & Onishi, T. 2017, *ApJ*, 837, 154
- Nakanishi, H., & Sofue, Y. 2006, *PASJ*, 58, 847
- . 2016, *PASJ*, 68, 5
- Nguyen Luong, Q., Motte, F., Schuller, F., et al. 2011, *A&A*, 529, A41
- Ortiz-León, G. N., Dzib, S. A., Kounkel, M. A., et al. 2017, *ApJ*, 834, 143
- Peek, J. E. G., Heiles, C., Douglas, K. A., et al. 2011, *ApJS*, 194, 20
- Pety, J. 2005, in *SF2A-2005: Semaine de l’Astrophysique Française*, ed. F. Casoli, T. Contini, J. M. Hameury, & L. Pagani, (Les Ulis: EDP), 721
- Quireza, C., Rood, R. T., Bania, T. M., Balser, D. S., & Maciel, W. J. 2006, *ApJ*, 653, 1226
- Reich, W., Fuerst, E., Reich, P., & Reif, K. 1990, *A&AS*, 85, 633
- Reid, M. J., Menten, K. M., Brunthaler, A., et al. 2014, *ApJ*, 783, 130
- Rigby, A. J., Moore, T. J. T., Plume, R., et al. 2016, *MNRAS*, 456, 2885
- Roman-Duval, J., Heyer, M., Brunt, C. M., et al. 2016, *ApJ*, 818, 144
- Sato, M., Reid, M. J., Brunthaler, A., & Menten, K. M. 2010, *ApJ*, 720, 1055
- Schuller, F., Csengeri, T., Urquhart, J. S., et al. 2017, *A&A*, 601, A124
- Shan, W., Yang, J., Shi, S., et al. 2012, *ITTST*, 2, 593
- Shimoikura, T., Dobashi, K., Nakamura, F., Shimajiri, Y., & Sugitani, K. 2018, *PASJ*, arXiv:1809.09855
- Sofue, Y., Kohno, M., Torii, K., et al. 2018, *PASJ*, arXiv:1807.06232
- Su, H., Tian, W., Zhu, H., & Xiang, F. Y. 2014a, in *IAU Symp.*, Vol. 296, *Supernova Environmental Impacts*, ed. A. Ray & R. A. McCray, (Cambridge: Cambridge Univ. Press), 372–373
- Su, Y., Fang, M., Yang, J., Zhou, P., & Chen, Y. 2014b, *ApJ*, 788, 122
- Su, Y., Sun, Y., Li, C., et al. 2016, *ApJ*, 828, 59
- Su, Y., Yang, J., Zhou, X., Zhou, P., & Chen, Y. 2014c, *ApJ*, 796, 122
- Su, Y., Zhang, S., Shao, X., & Yang, J. 2015, *ApJ*, 811, 134
- Su, Y., Zhou, X., Yang, J., et al. 2017a, *ApJ*, 845, 48

- . 2018, *ApJ*, 863, 103
- . 2017b, *ApJ*, 836, 211
- Sun, J. X., Lu, D. R., Yang, J., et al. 2018a, *AcASn*, 59, 3
- Sun, Y., Su, Y., Zhang, S.-B., et al. 2017, *ApJS*, 230, 17
- Sun, Y., Xu, Y., Fang, M., et al. 2018b, *ApJ*, 869, 148
- Sun, Y., Xu, Y., Yang, J., et al. 2015, *ApJL*, 798, L27
- Umemoto, T., Minamidani, T., Kuno, N., et al. 2017, *PASJ*, 69, 78
- Wang, C., Yang, J., Xu, Y., et al. 2017, *ApJS*, 230, 5
- Wenger, T. V., Khan, A. A., Ferraro, N. G., et al. 2018, *ApJ*, 852, 2
- Xiong, F., Chen, X., Yang, J., et al. 2017, *ApJ*, 838, 49
- Xu, Y., Hou, L. G., & Wu, Y. W. 2018, *RAA*, 18, 146
- Zhan, X.-L., Jiang, Z.-B., Chen, Z.-W., Zhang, M.-M., & Song, C. 2016, *RAA*, 16, 56
- Zhang, B., Zheng, X. W., Reid, M. J., et al. 2009, *ApJ*, 693, 419
- Zhang, B., Moscadelli, L., Sato, M., et al. 2014a, *ApJ*, 781, 89
- Zhang, S., Xu, Y., & Yang, J. 2014b, *AJ*, 147, 46
- Zhou, X., Yang, J., Fang, M., & Su, Y. 2014, *ApJ*, 791, 109
- Zhou, X., Yang, J., Fang, M., et al. 2016, *ApJ*, 833, 4

Table 1. Parameters of the MWISP Survey Data

Molecular lines	^{12}CO ($J=1-0$)	^{13}CO and C^{18}O ($J=1-0$)
HPBW	$\sim 49''$	$\sim 52''$
Grid spacing	$30''$	$30''$
Velocity separation	0.16 km s^{-1}	0.17 km s^{-1}
System temperature	$\sim 250 \text{ K}$	$\sim 140 \text{ K}$
rms (T_{MB})	$\sim 0.5 \text{ K}$	$\sim 0.3 \text{ K}$
Mapping regions	$25^\circ.8 \lesssim l \lesssim 49^\circ.7, b \lesssim 5^\circ.2$	$25^\circ.8 \lesssim l \lesssim 49^\circ.7, b \lesssim 5^\circ.2$

Table 2. Two Gaussian Components for the Inner Galactic CO Plane

Narrow			Broad			χ^2/dof
z_0 (pc)	FWHM (pc)	I_0 (K km s^{-1})	FWHM (pc)	I_0 (K km s^{-1})		
-11.3	88.5	40.9	276.8	20.8	60.5/84 ^a	

^aThe residual is calculated with a weight of the mean CO intensity per bin.

NOTE— z_0 is the displacement of the CO gas from the Galactic plane of $b = 0^\circ$; FWHM is the thickness of the CO layer; I_0 is the peak of the best fit. Note that the zero-point is at 3.8 K km s^{-1} , i.e., $I_0 = I_{\text{peak}} = I(z_0) + 3.8 \text{ K km s}^{-1}$ (see Figure 17 and the text). Note that the z_0 value of the broad component is fixed to that of the narrow one. Samples are from the CO emission near the tangent point, i.e., $V_{\text{LSR}} > 60 \text{ km s}^{-1}$.

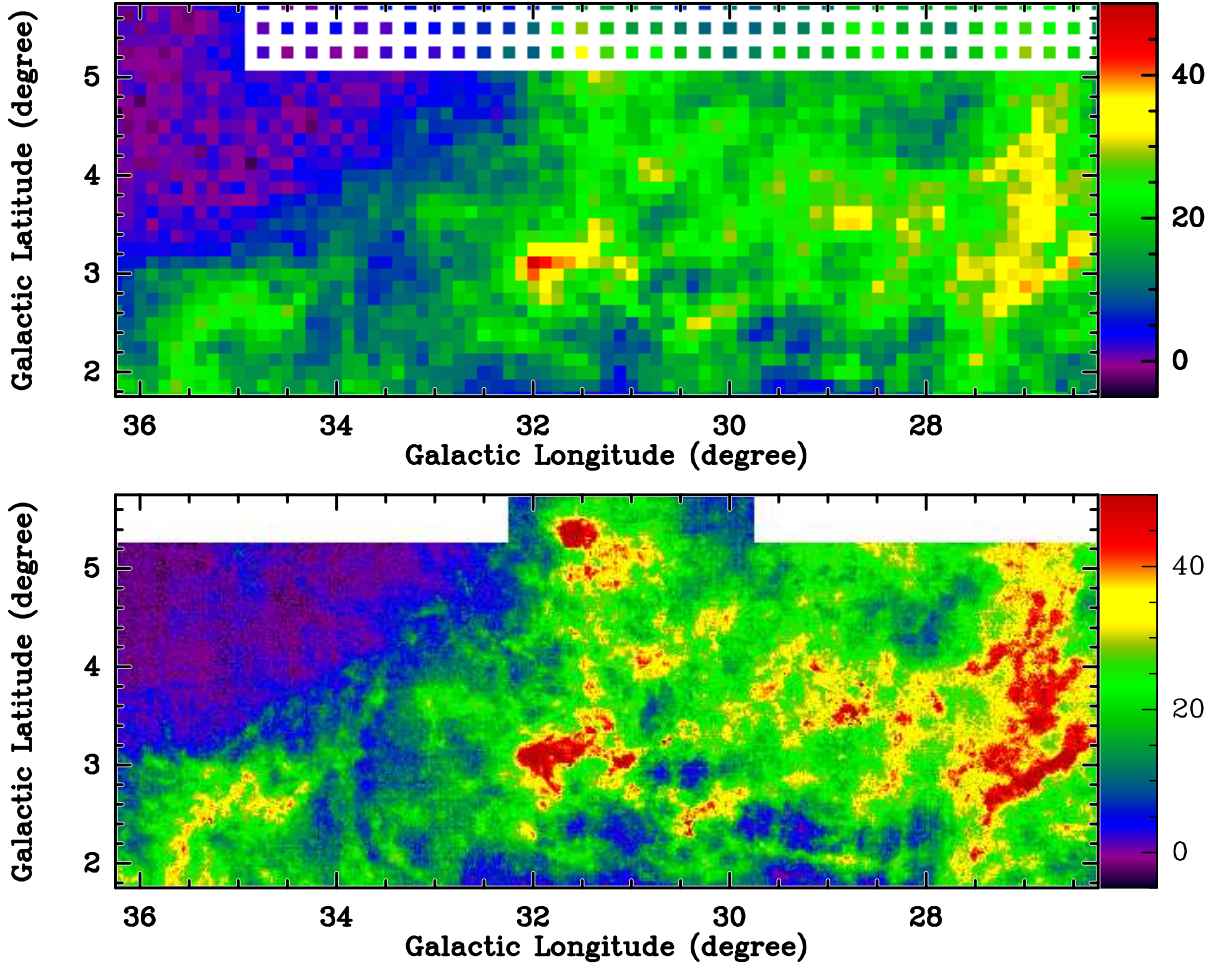


Figure 1. Top: The ^{12}CO integrated intensity map of the Serpens/Aquila Rift MC complex from the Columbia-CfA CO survey (Dame et al. 2001). Bottom: The MWISP ^{12}CO integrated intensity map for the same region. In both panels, all the integrated velocity ranges are 0 to 30 km s^{-1} , and the color bars represent the integrated intensity in units of K km s^{-1} .

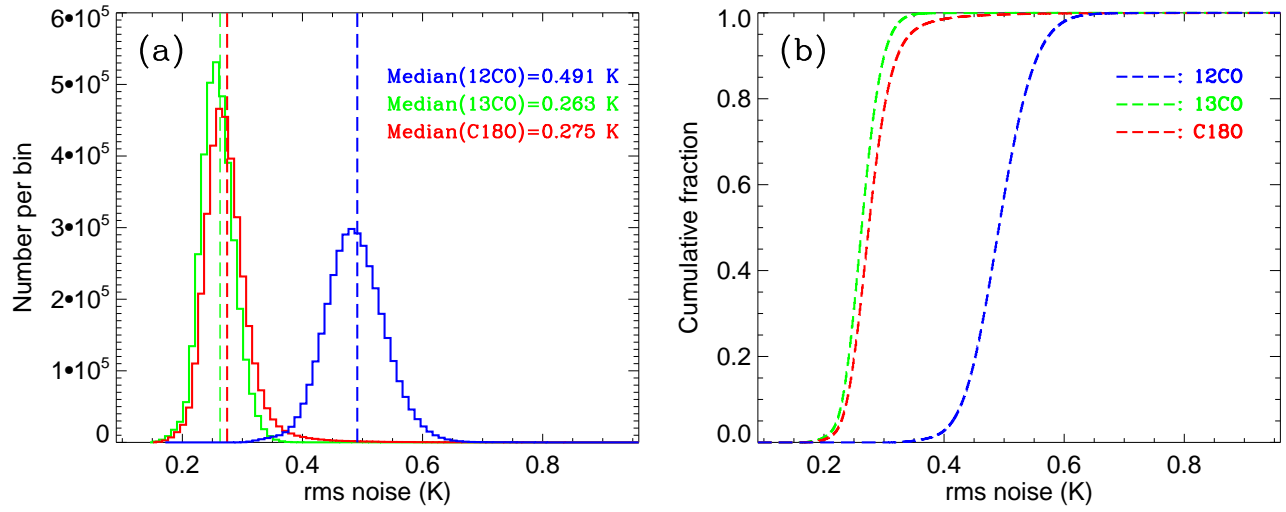


Figure 2. (a): Distribution of rms noise values of the three lines for the whole dataset. The long-dashed lines indicate the median values of ^{12}CO ($J=1-0$) (blue), ^{13}CO ($J=1-0$) (green), and C^{18}O (red) emission, respectively. (b): Cumulative distribution of rms noise values for the three CO lines.

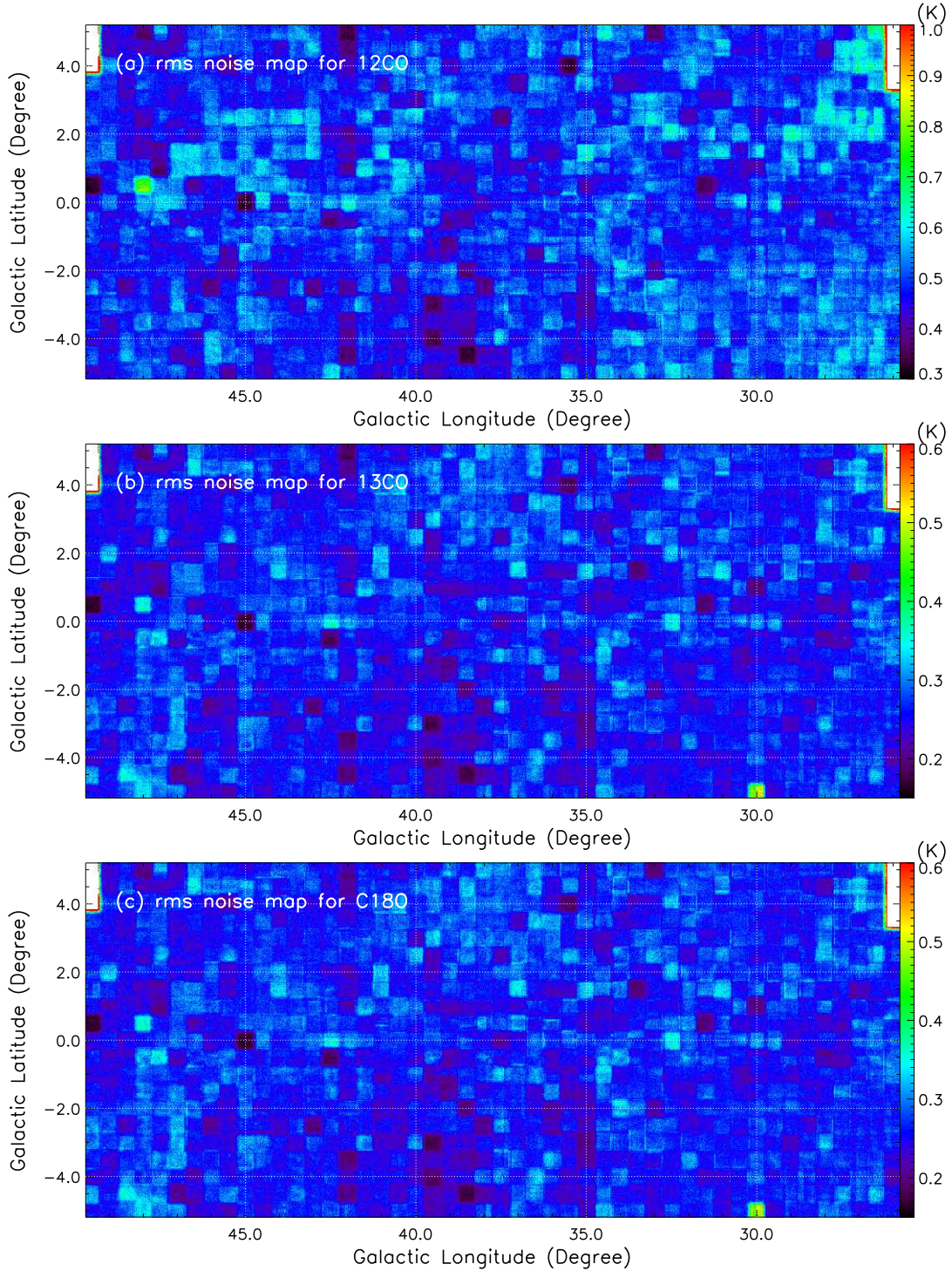


Figure 3. Rms noise maps for the ^{12}CO , ^{13}CO , and C^{18}O ($J=1-0$) lines. The maps display the variation in rms between cells. There are some stripes along l and b in the maps due to the bad weather (or the high system temperature) in the OTF mapping.

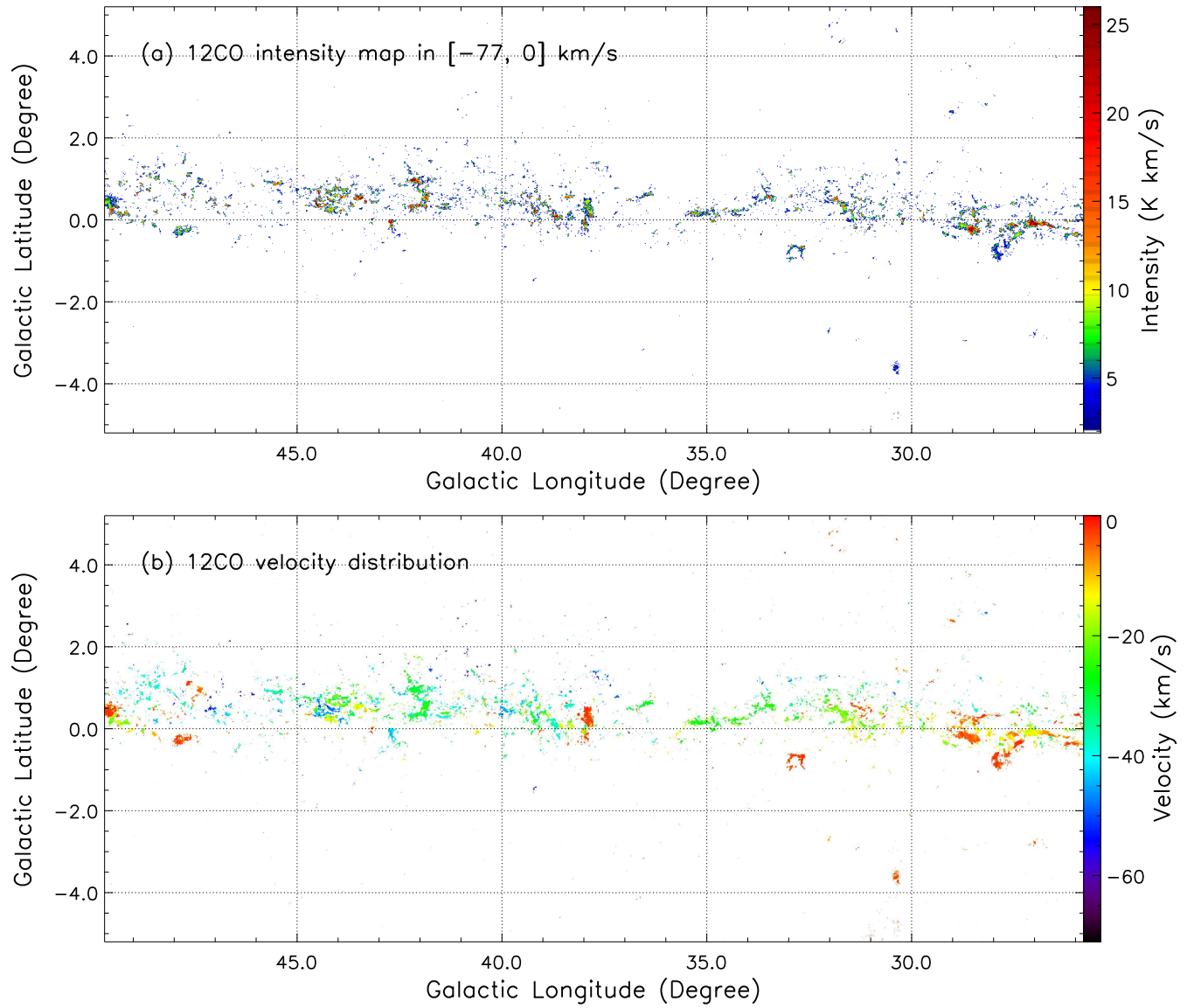


Figure 4. (a) Integrated emission of the ^{12}CO ($J=1-0$) emission in the interval of -77 to 0 km s^{-1} . (b) Intensity-weighted mean velocity (first moment) map of the ^{12}CO emission for $V_{\text{LSR}} \leq 0$ km s^{-1} MCs.

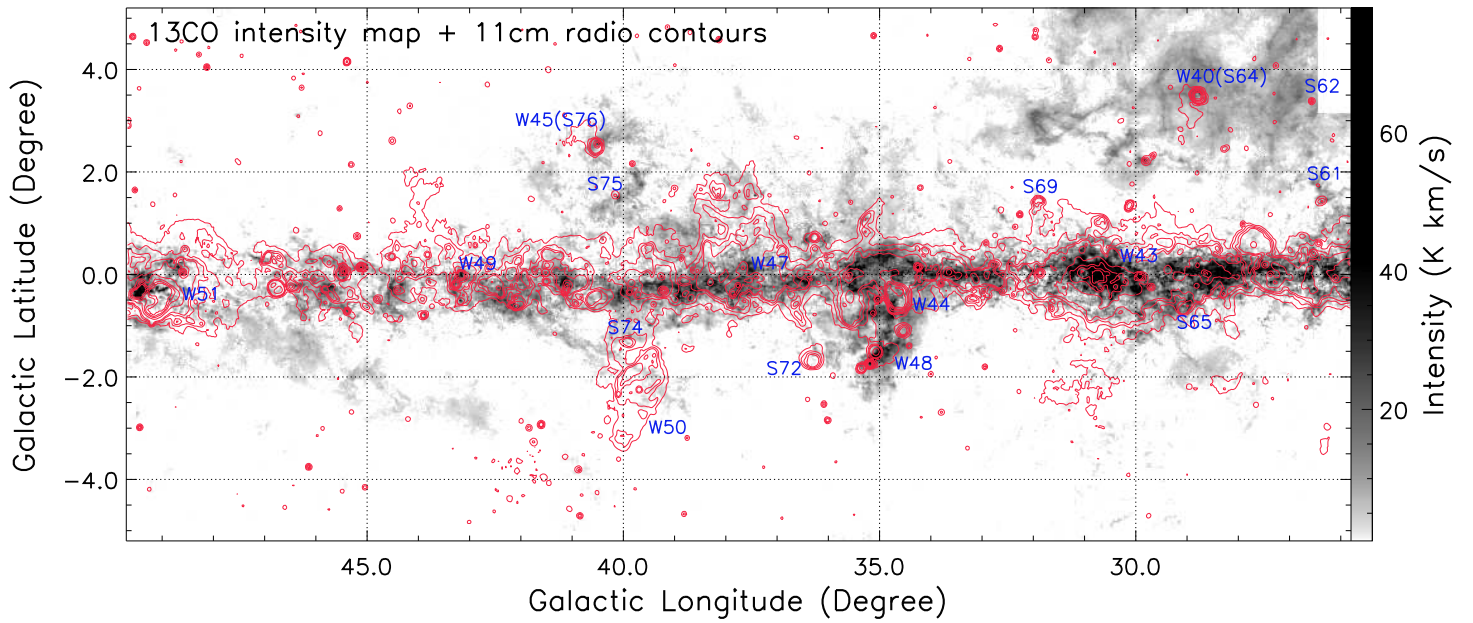


Figure 5. MWISP ^{13}CO ($J=1-0$) intensity map in the 0–130 km s^{-1} interval, overlaid with the Effelsberg 11 cm radio contours (250, 500, 750, 1×10^3 , 2.5×10^3 , 5×10^3 , 7.5×10^3 , and 1×10^4 mK) from Reich et al. (1990). Some bright and/or extended radio sources are labeled on the map.

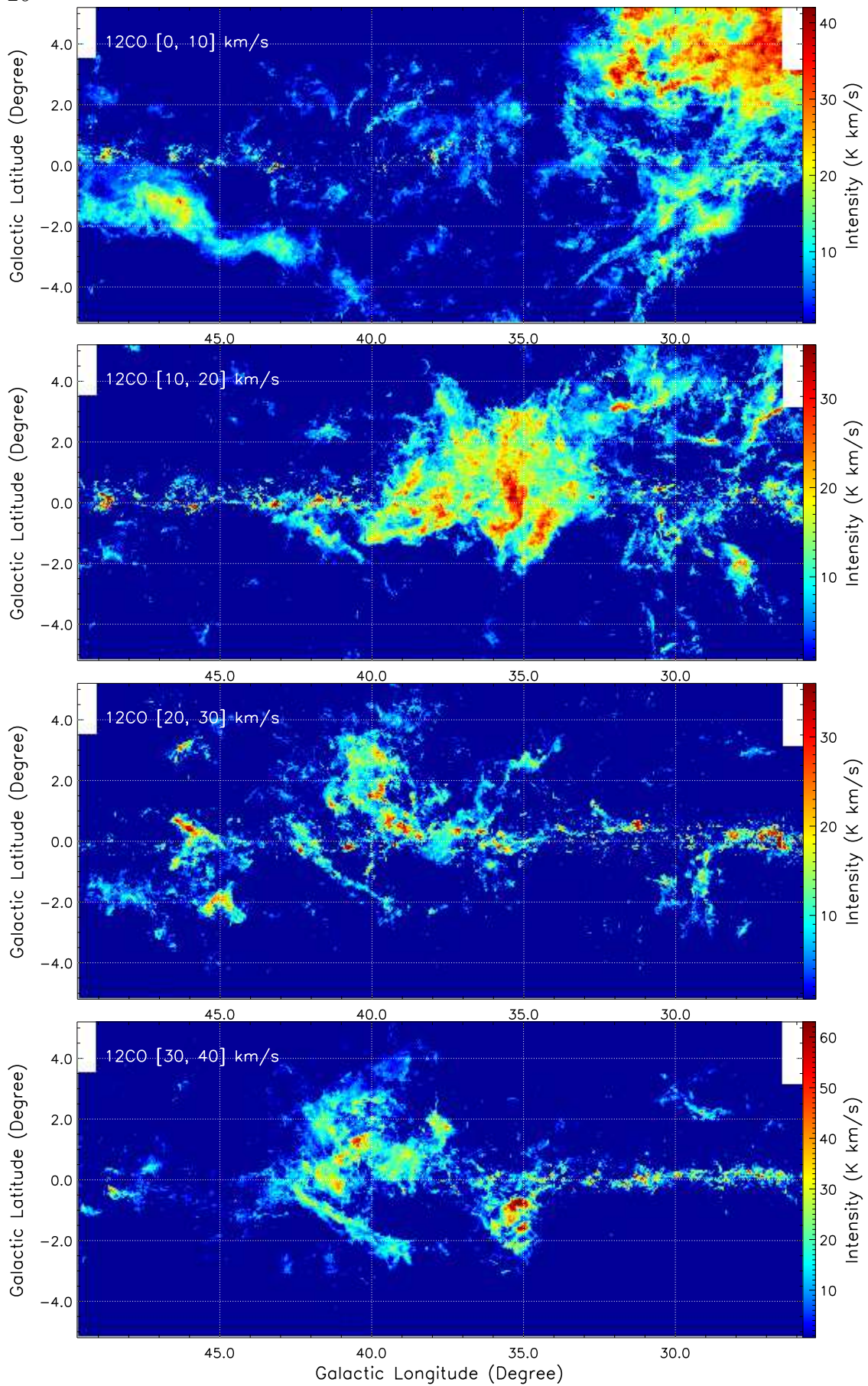


Figure 6. Channel maps of ^{12}CO with velocity intervals of 10 km s^{-1} for $V_{\text{LSR}} \geq 0 \text{ km s}^{-1}$ gas.

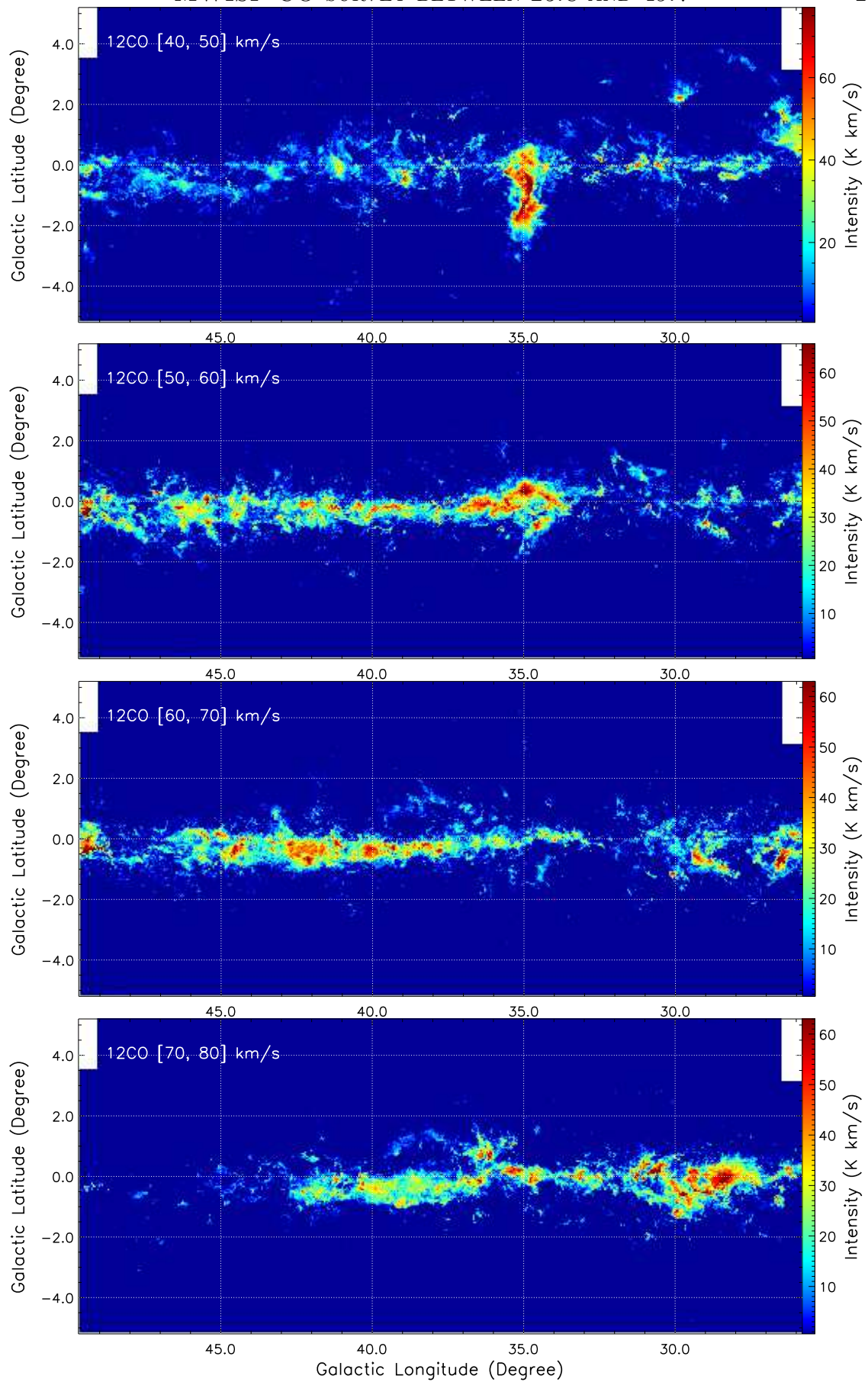


Figure 6. (Continued)

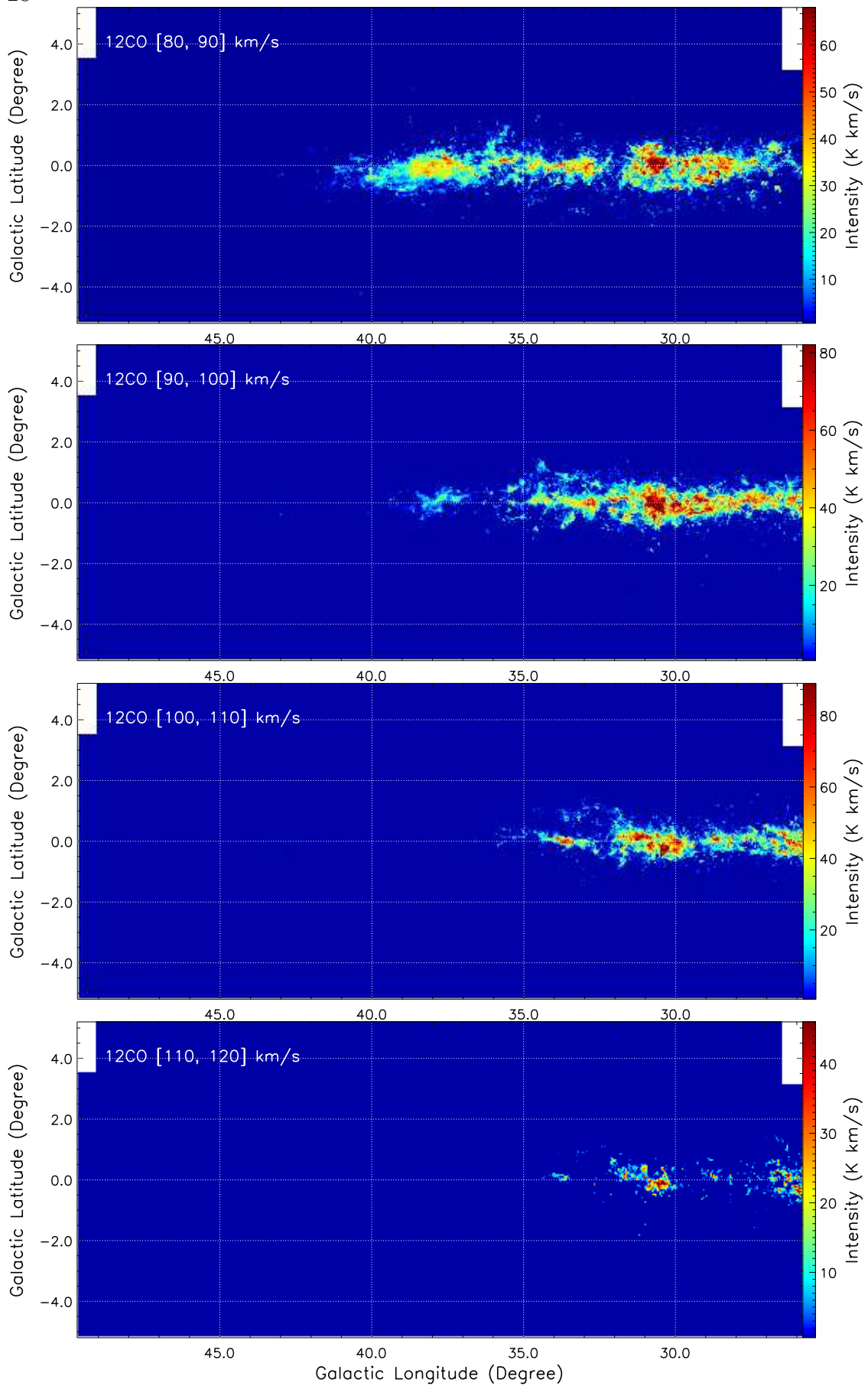


Figure 6. (Continued)

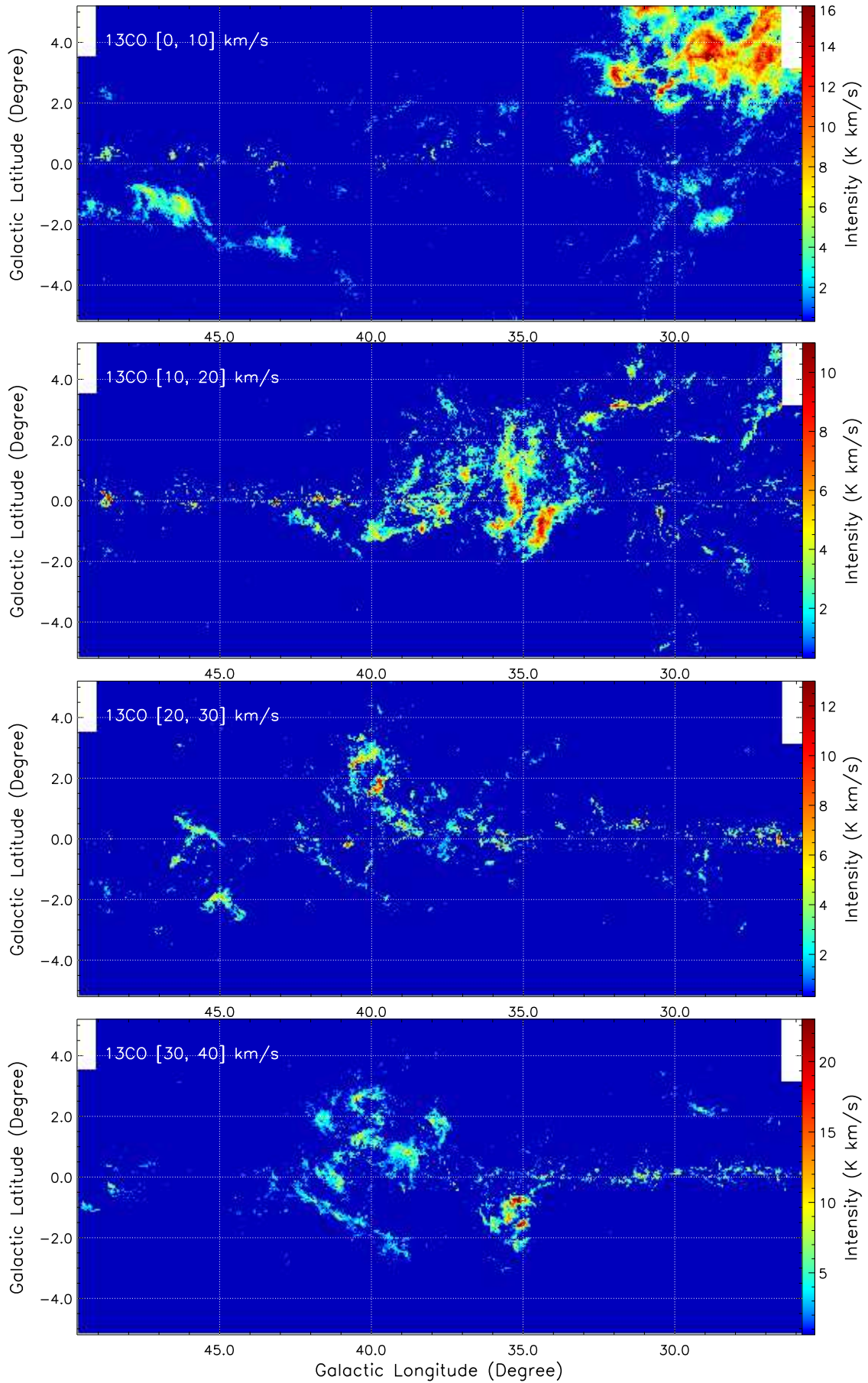


Figure 7. Channel maps of ^{13}CO with velocity intervals of 10 km s^{-1} for $V_{\text{LSR}} \geq 0 \text{ km s}^{-1}$ gas.

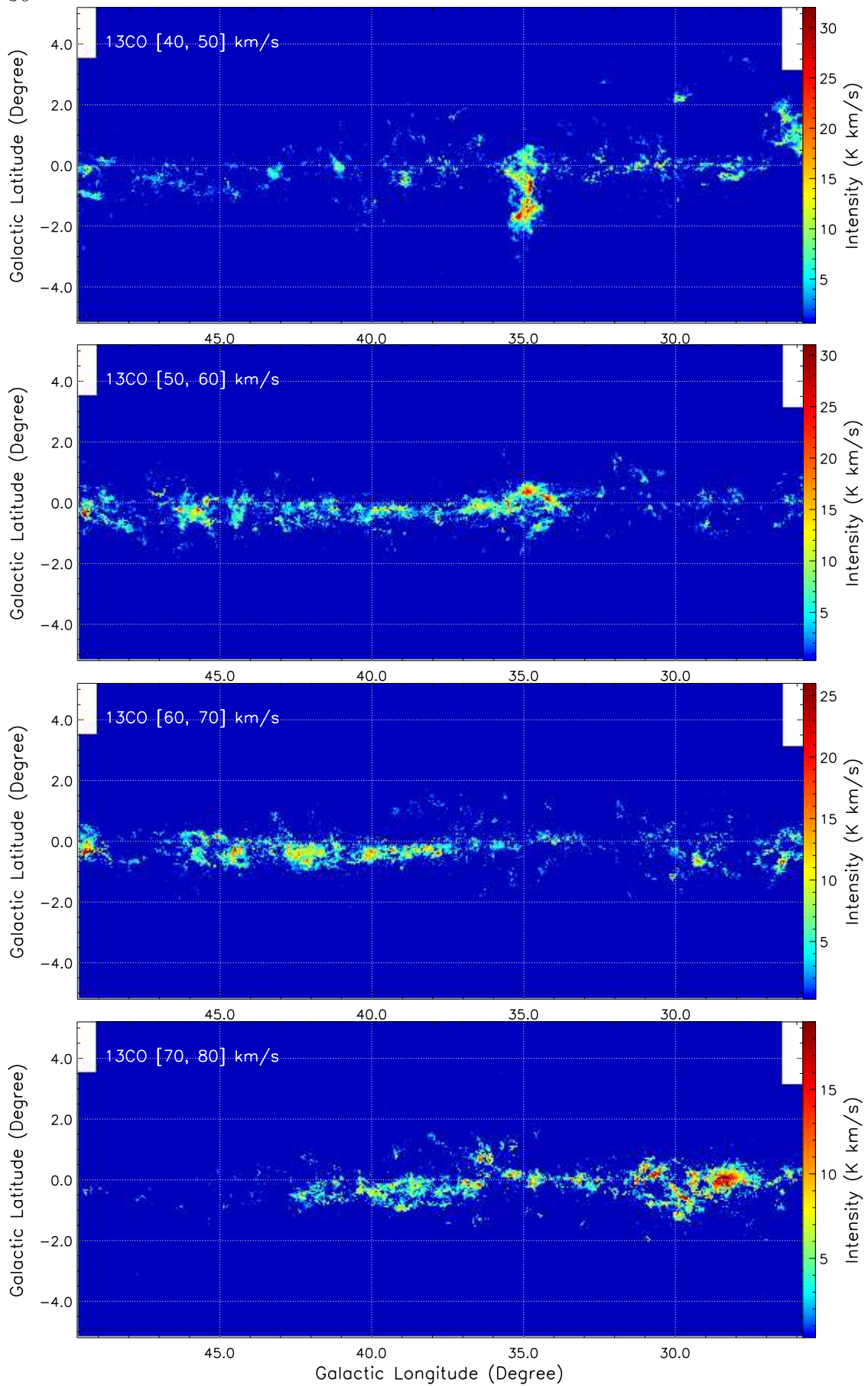


Figure 7. (Continued)

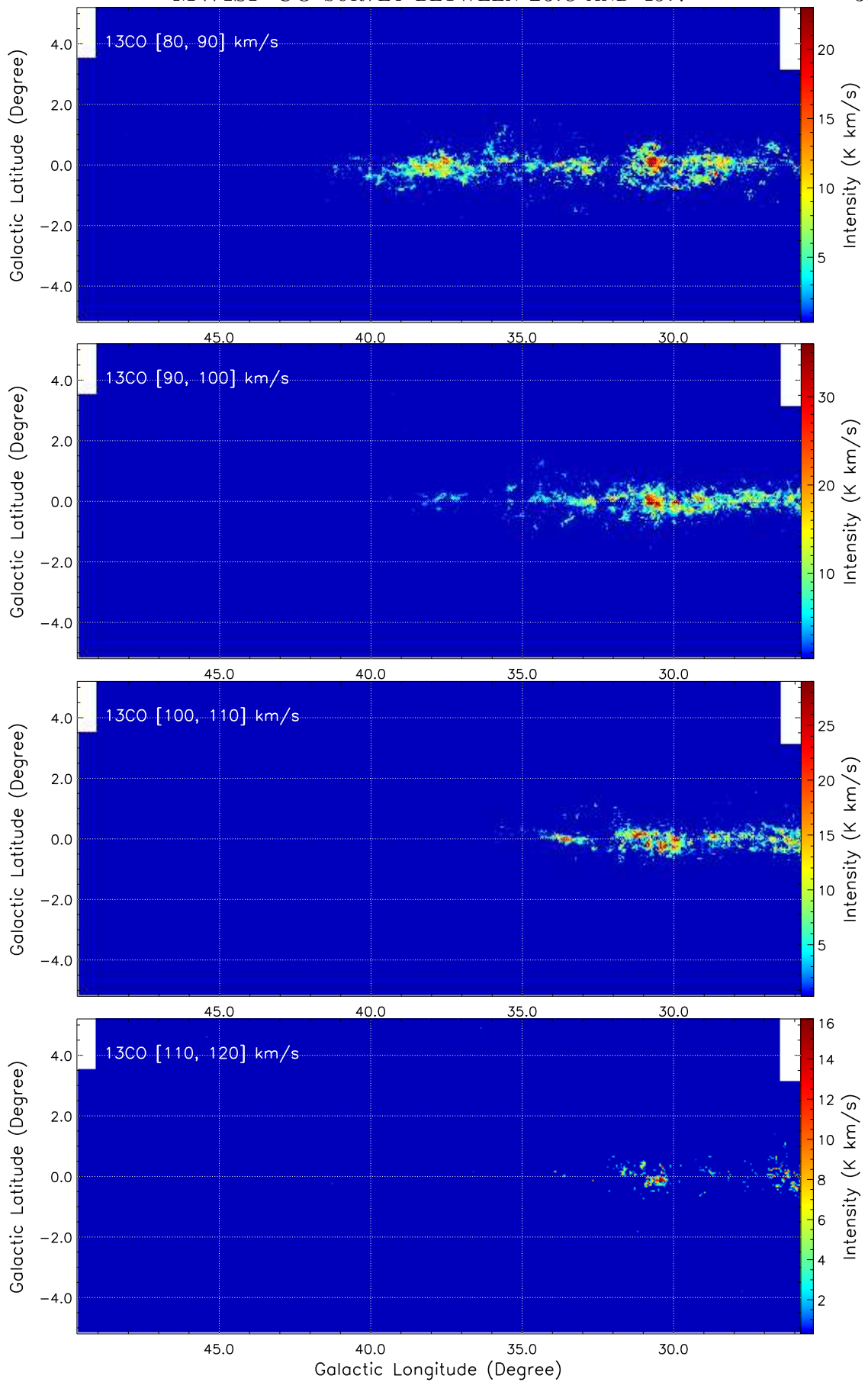


Figure 7. (Continued)

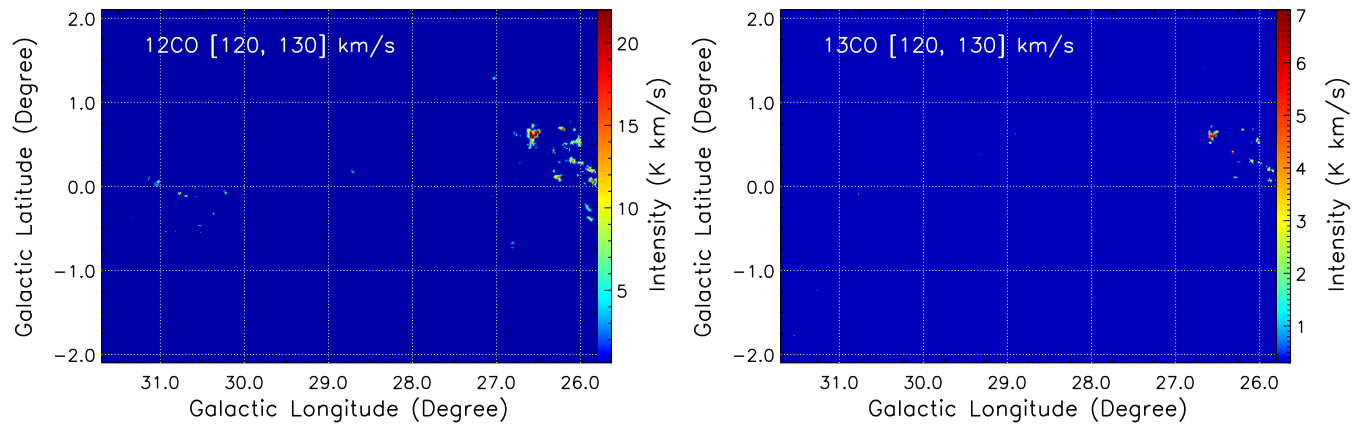


Figure 8. Left panel: The integrated emission of the ^{12}CO emission in the interval of 120 to 130 km s^{-1} . Right panel: The integrated emission of the ^{13}CO emission in the same interval.

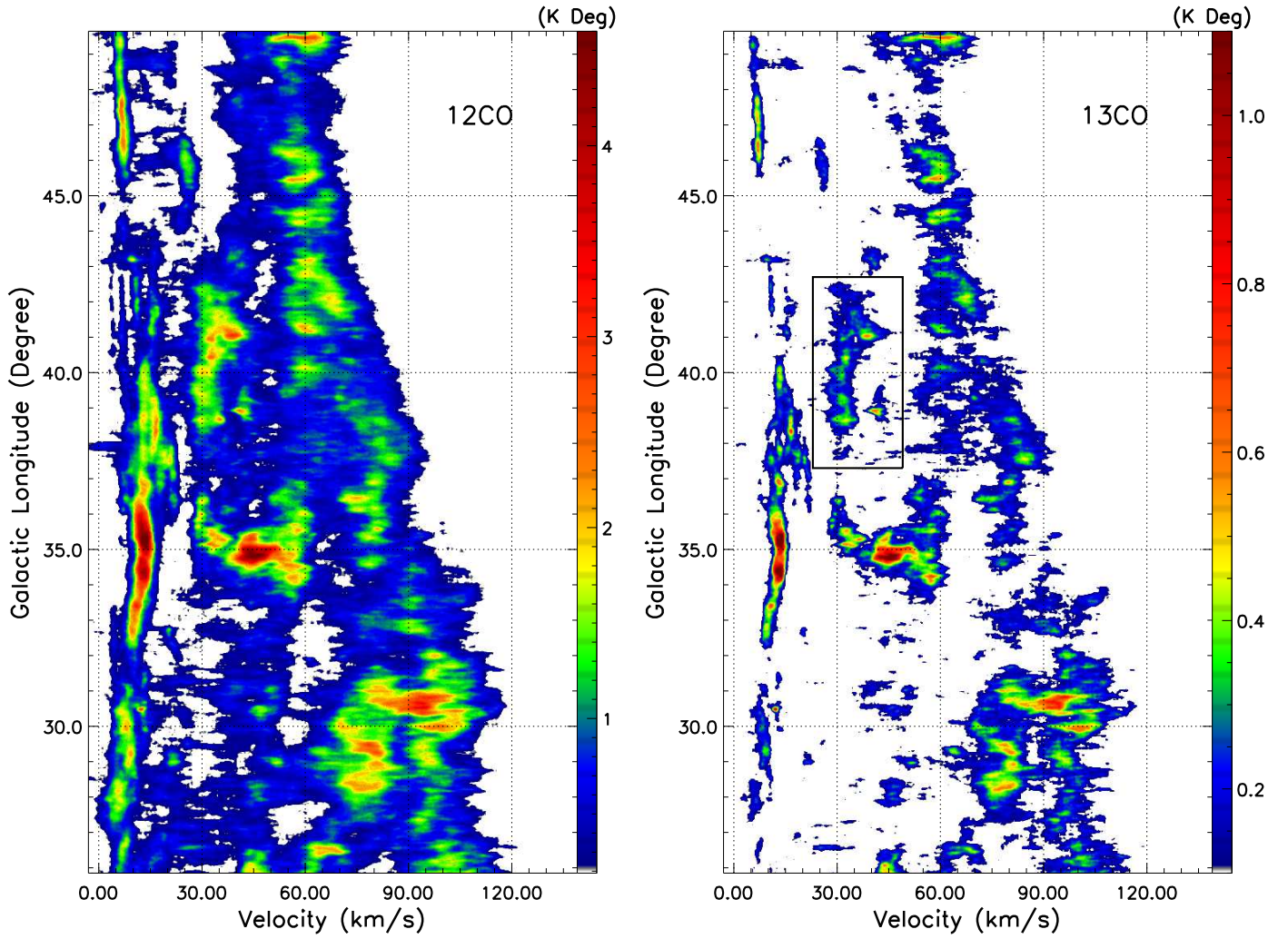


Figure 9. Longitude–velocity diagrams of the ^{12}CO and ^{13}CO emission for $V_{\text{LSR}} \geq 0 \text{ km s}^{-1}$ gas. The rectangle in the right panel shows the region of the dense molecular gas associated with H II regions Sh 2-75 and Sh 2-76, which was not fully covered in latitude by the GRS survey (Jackson et al. 2006).

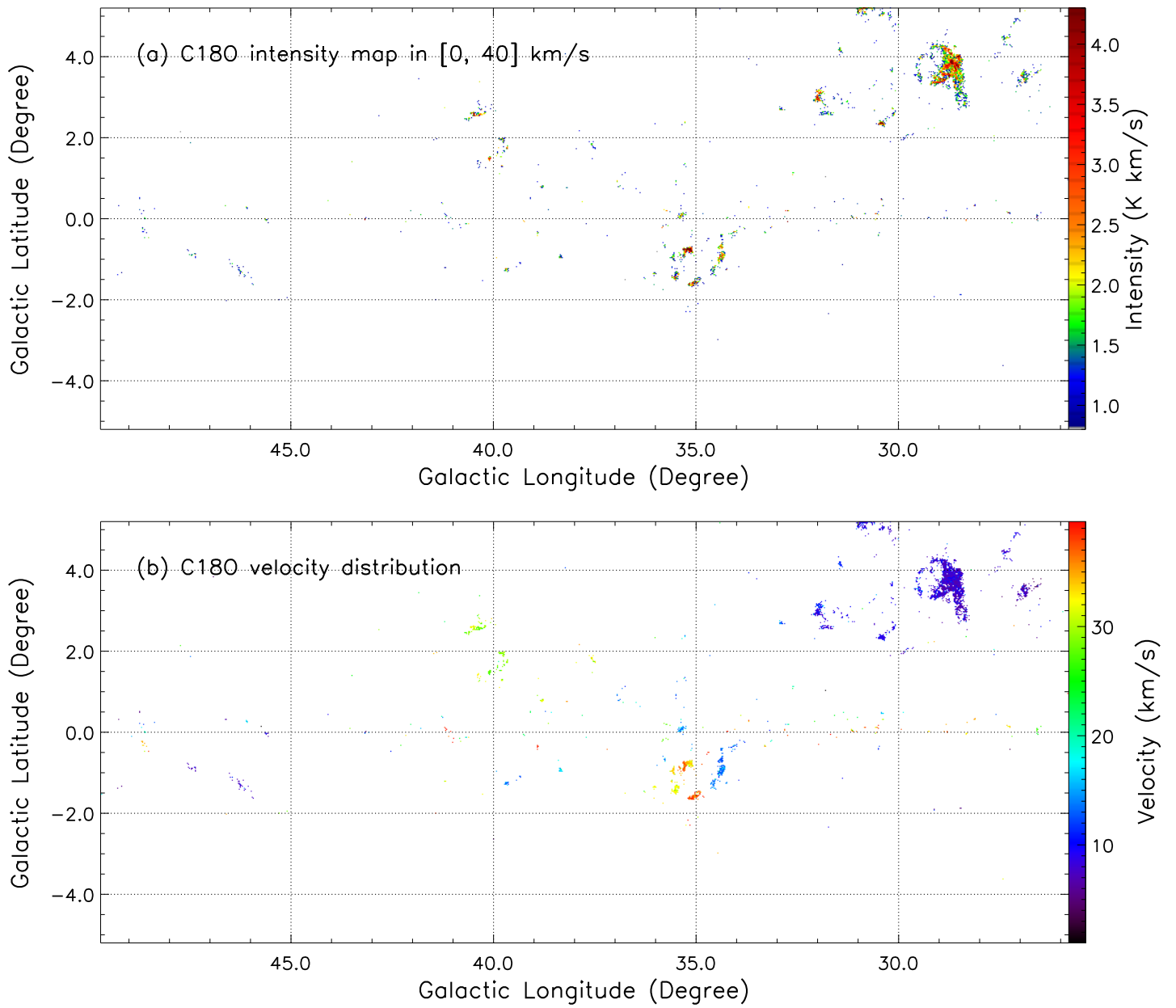


Figure 10. Intensity map and velocity distribution of $C^{18}O$ emission for $V_{LSR}=0-40$ km s^{-1} gas.

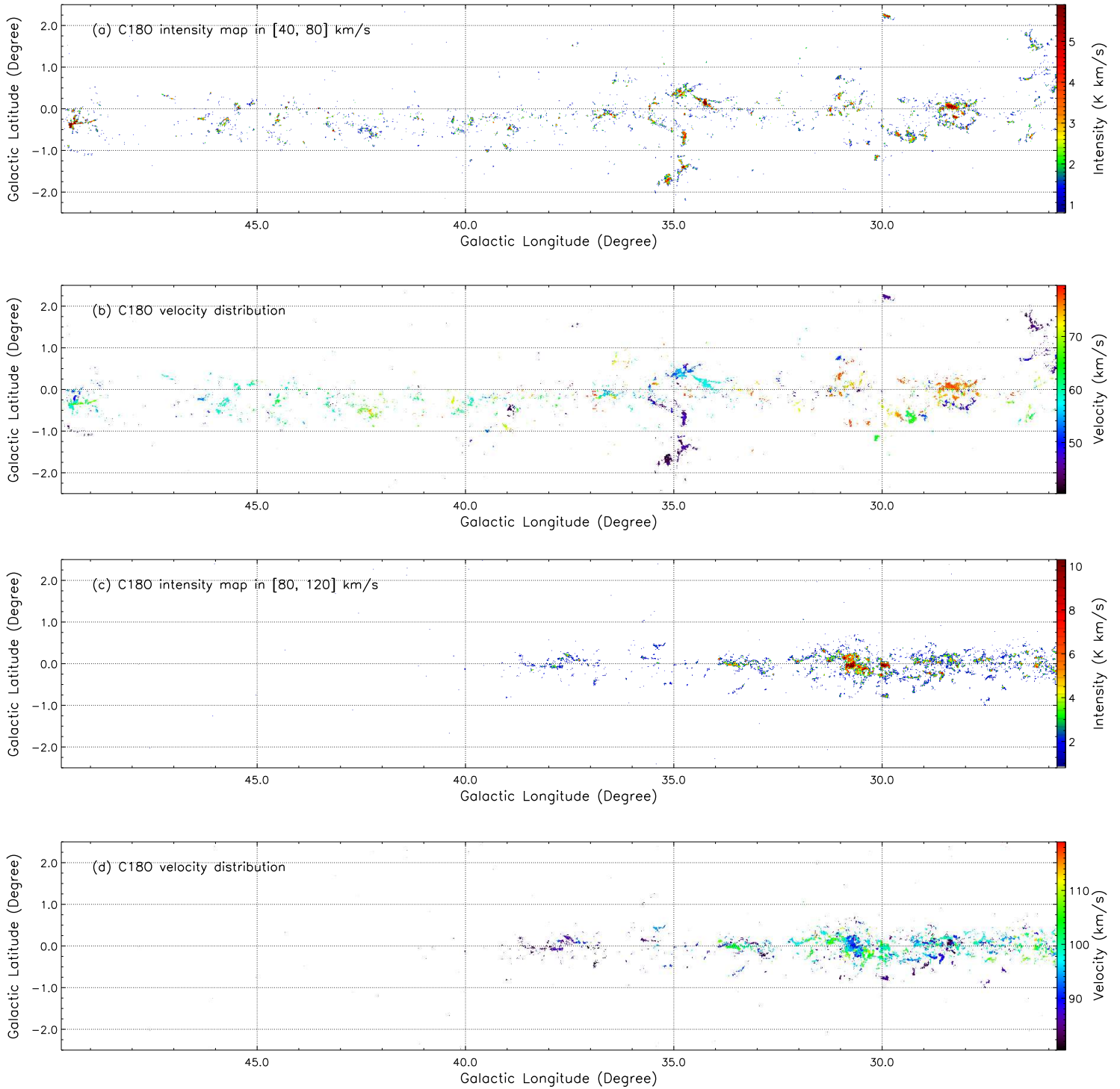


Figure 11. Intensity map and velocity distribution of $C^{18}O$ emission for $V_{LSR}=40$ – 80 km s^{-1} and 80 – 120 km s^{-1} gas.

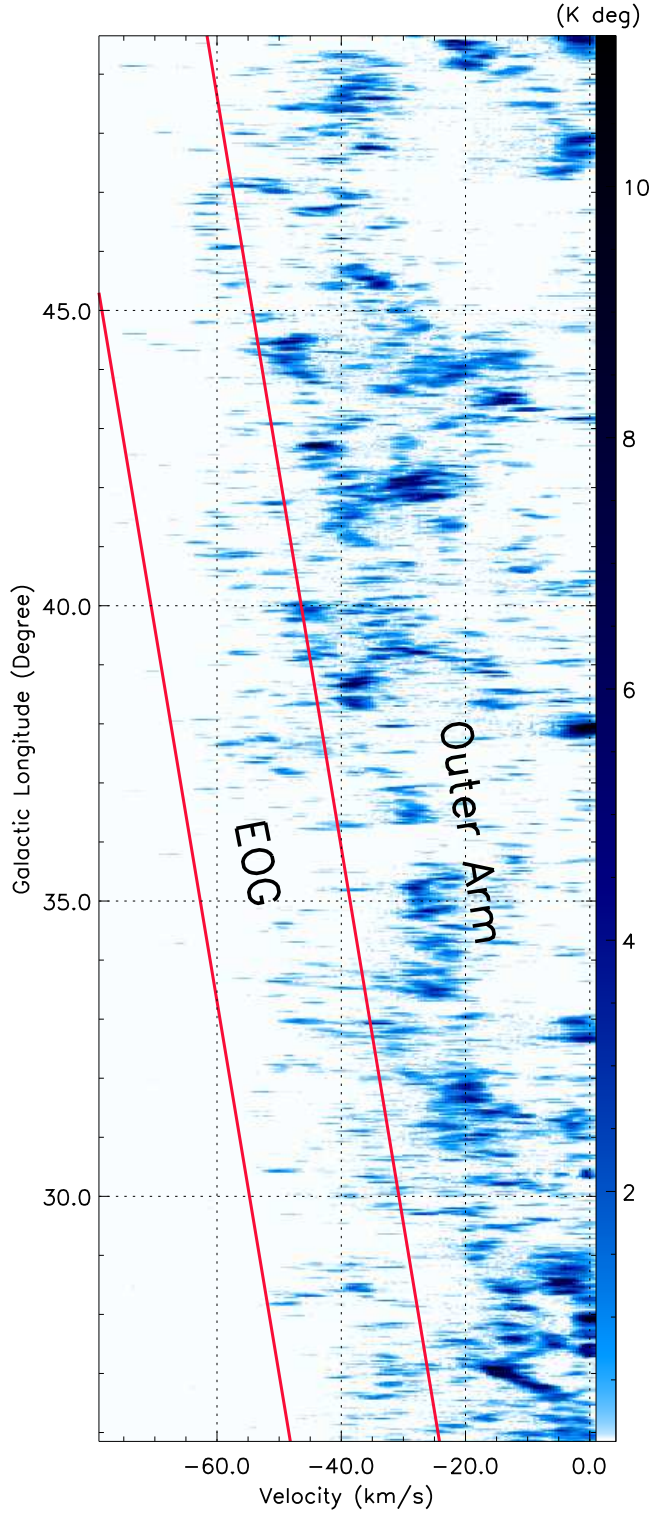


Figure 12. Longitude–velocity diagram of the ^{12}CO emission for $V_{\text{LSR}} \lesssim 0 \text{ km s}^{-1}$ gas. The region between the red lines ($V_{\text{LSR}} = -1.57 \times l + 4.34 \pm 12 \text{ km s}^{-1}$) contains most of the detected CO gas in the EOG. The Outer Arm and the EOG regions are labeled on the map. Note that the ^{12}CO signal is multiplied by a factor of 100 for the corresponding velocity range due to the weak emission of the distant MCs (see the text).

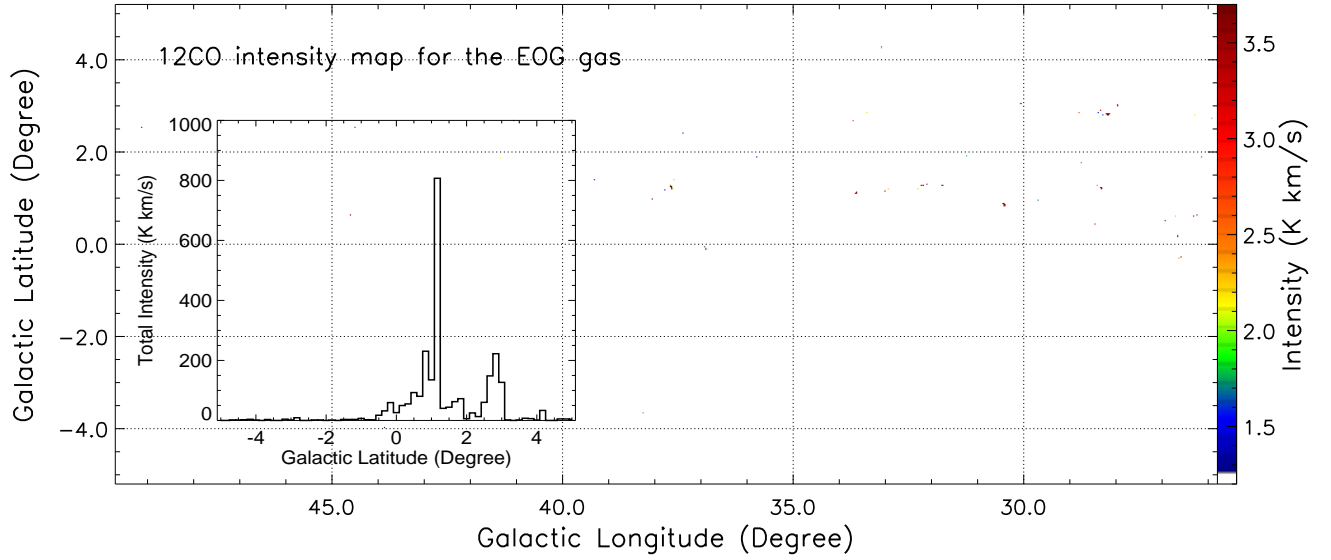


Figure 13. Distribution of the EOG ^{12}CO emission with $V_{\text{LSR}} \lesssim -1.57 \times l + 4.34 \text{ km s}^{-1}$. The CO intensity less than 1.2 K km s^{-1} (or $\sim 3\sigma$ for a typical velocity range of 4 km s^{-1}) is not shown on the map. Two intensity peaks are found to be at $b \sim 1^\circ.2$ and $b \sim 2^\circ.8$. Note that the MC at ($l = 40^\circ.875$, $b = 1^\circ.250$, $V_{\text{LSR}} \sim -57 \text{ km s}^{-1}$; e.g., Table 1 in [Dame & Thaddeus 2011](#)) cannot be seen in the map because of the velocity criterion here. But the MC probably belongs to the EOG. The corresponding CO emission of the distant MC can be seen in Figures 4 and 12.

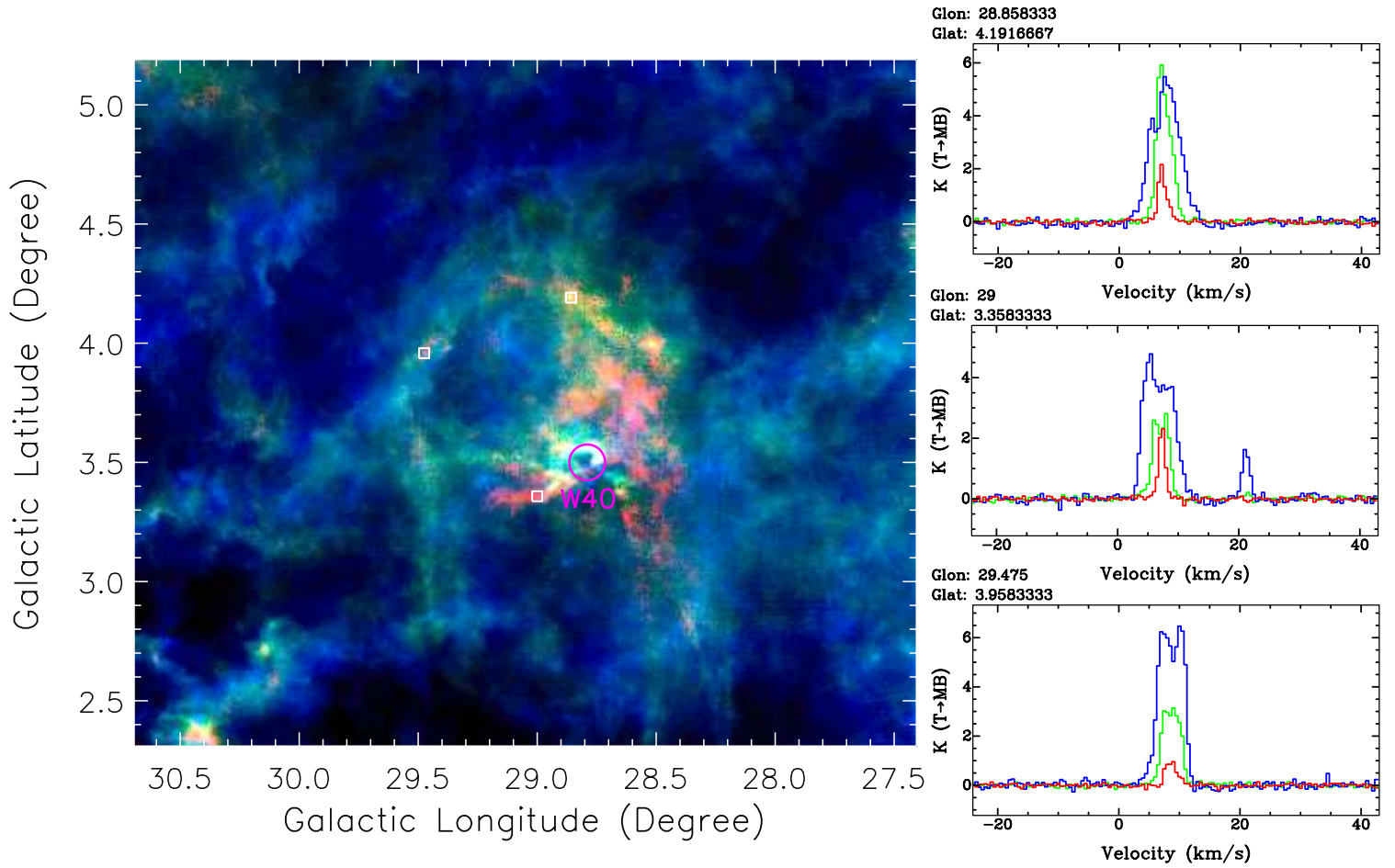


Figure 14. ^{12}CO ($J=1-0$, blue), ^{13}CO ($J=1-0$, green), and C^{18}O ($J=1-0$, red) intensity map in the $1-14 \text{ km s}^{-1}$ interval toward the H II region W40. The H II region W40 is marked as a purple circle centered at $l = 28^\circ 8'$, $b = 3^\circ 5'$ with a diameter of $9'$ (e.g., Quireza et al. 2006). Typical spectra, which are extracted from the three white boxes, are shown to the right of the map.

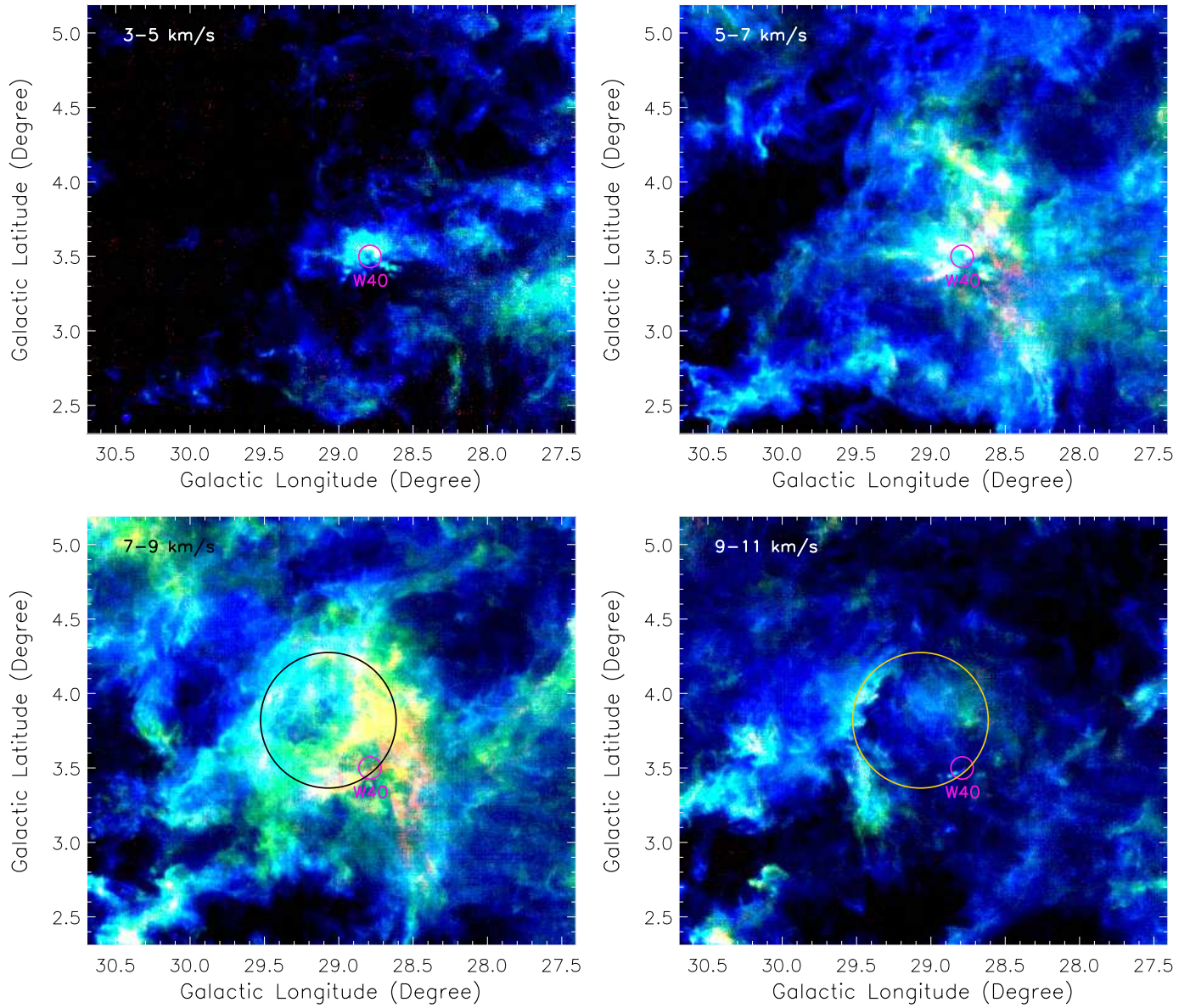


Figure 15. Channel maps of ^{12}CO ($J=1-0$, blue), ^{13}CO ($J=1-0$, green), and C^{18}O ($J=1-0$, red) with velocity intervals of 3–5, 5–7, 7–9, and 9–11 km s^{-1} toward the W40 complex. The large circle, which is centered at ($l=29^{\circ}07$, $b=3^{\circ}82$) with a radius of $0^{\circ}.45$, displays the bubble-like dense gas structure toward the complex.

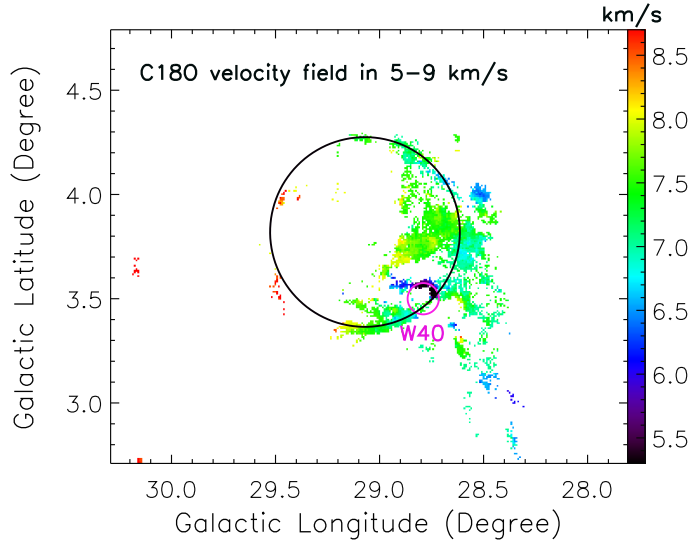


Figure 16. C^{18}O velocity field toward the W40 region. The big and small circles are the same as those in Figure 15. Samples with $T_{\text{MB}}(\text{C}^{18}\text{O}) \gtrsim 5\sigma$ are considered here.

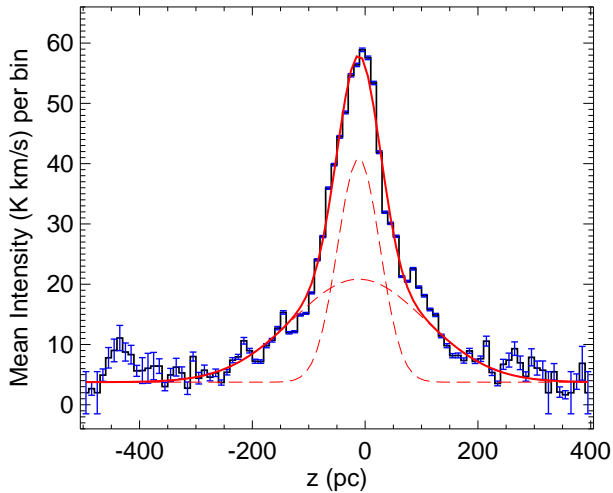


Figure 17. CO distribution along the distance from the Galactic plane of $b = 0^\circ$. The two red dashed lines indicate the narrow and broad Gaussian components, respectively. The error bars, which were calculated from $I_{\text{mean}}(\text{CO})/(\text{number of pixels per bin})^{0.5}$, are shown in blue. Note that the zero-point of the best fitting is at 3.8 K km s^{-1} according to the MWISP CO data (see Table 2). The unusual peak at $z \sim -435 \text{ pc}$ probably has a connection with the dynamical interactions between the jets of the unique microquasar SS 433 in W50 and the surrounding high- z gas (see the text).